A STUDY OF THE FIELD INDUCED SPECTRUM OF HYDROGEN AT HIGH RESOLUTION

by

HENDRICUS LEONARDUS BUIJS

B.A.Sc., University of Toronto, 1963

M.Sc., University of Toronto, 1966

A THESIS SUBMITTED IN PARTIAL FULFILMENT OF THE REQUIREMENTS FOR THE DEGREE OF

DOCTOR OF PHILOSOPHY

in the Department

of

PHYSICS

We accept this thesis as conforming to the required standard.

THE UNIVERSITY OF BRITISH COLUMBIA

December, 1969

In presenting this thesis in partial fulfilment of the requirements for an advanced degree at the University of British Columbia, I agree that the Library shall make it freely available for reference and study. I further agree tha permission for extensive copying of this thesis for scholarly purposes may be granted by the Head of my Department or by his representatives. It is understood that copying or publication of this thesis for financial gain shall not be allowed without my written permission.

Department of PHYSICS

The University of British Columbia
Vancouver 8, Canada

Date Feb 3 /70

ABSTRACT

The static field induced absorption spectrum of hydrogen has been investigated at high resolution and with reliable frequency calibration over the density range from 1.5 amagat to 28 amagat. Frequencies have been extrapolated to zero density in order to obtain molecular constants for the isolated molecule. Line profiles have been compared with various functions and the simple dispersion profile seems to fit the data best over the density range studied. The linewidth, however, decreases with density until it reaches a minimum at about 2.5 amagat below which it starts to increase again. The minimum width is about 4 times less than the width of the classical doppler line. This behaviour of the line width is consistent with the phenomena of "collision narrowing" in the infrared. From the intensities of the lines we obtain the isotropic polarizability $(\alpha)_{1-0} = 1.21\ cm^3$.

TABLE OF CONTENTS

LIST OF FIGURES

FIGURE

LIST OF TABLES

ACKNOWLEDGEMENT

It is a pleasure to express my gratitude to my supervisor, Dr. H.P. Gush, for always giving the advice needed in particular during difficult moments.

I also like to extend my gratitude to the staff of the computation center for their patience and understanding despite the heavy demands put on their duties during data analysis.

INTRODUCTION

The spectrum of the hydrogen molecule has been extensively investigated in the ultraviolet and the infrared regions as well as by the Raman effect. In spite of this it was deemed worthwhile to reinvestigate the infrared spectrum of hydrogen because new techniques have made it possible to measure the frequencies and shapes of spectral lines with considerably higher precision than was before possible. Indeed this investigation has borne fruit: in addition to obtaining highly precise frequencies for the hydrogen molecule, the phenomenon of collision narrowing of spectral lines has been studied in the infrared region for the first time.

The hydrogen molecule possesses a centre of symmetry and consequently the matrix elements of the electric dipole moment between different vibrational states equal zero. The molecule therefore does not display a "normal" infrared spectrum. An infrared spectrum due to quadrupole absorption is allowed, however, and has been observed using a long absorption path. An absorption in the fundamental frequency band also arises because of electric dipole moments induced in colliding pairs of molecules; this absorption spectrum is characterized by very broad spectral features and is not suitable for the determination of molecular frequencies, although it is of much importance in the study of intermolecular forces.

The hydrogen molecule can be made to exhibit an infrared dipole spectrum if it is placed in a static electric field which polarizes the molecule. This effect was first predicted by Condon (1932) and demonstrated experimentally by Crawford and Dagg (1953) and more recently by Crawford and MacDonald (1958), Terhune (1959), Church (1959) and Foltz et al (1966). It is this phenomenon which has been exploited in this work because the absorption is much stronger at easily realizable electric field strengths than is the quadrupole absorption. This means that an absorption spectrum can be measured at pressures of one atmosphere or less in an absorption cell of modest size, and an extrapolation to zero gas density of the observed absorption frequencies may be carried out with confidence. It was because measurements at this low density were possible, that the existence of collision narrowing was revealed.

The spectral measurements were carried out using a two-beam interferometer of one meter maximum path difference. This permitted measurements to be made with a limit of resolution of approximately 0.006 cm^{-1}, and line centres have been determined to within better than 0.002 cm^{-1}.

1. Experimental Procedure

A schematic drawing showing the overall experimental procedure is shown in Figure 1. Light from an incandescent lamp is passed through a polarizer and a special optical filter which selects bands of radiation in the vicinity of the hydrogen absorption lines. This radiation passes through the absorption cell where a static field is impressed on the gas, and it then enters a two beam interferometer. An infrared detector measures the intensity on the exit side of the interferometer; this intensity varies as the optical path difference in the interferometer is changed and gives rise to a signal which we call the interferogram. The interferogram is proportional to the autocorrelation function of the electric field of the radiation incident on the interferometer, and it is hence proportional to the Fourier Transform of the spectrum.* The optical path difference is monitored with interference fringes produced by light from a He-Ne laser which also passes through the interferometer. The interferogram is recorded on magnetic tape; this record is then read by an I.B.M. 360/67 computer and the Fourier transform is evaluated numerically. The ratio of two spectra, one obtained with the static field switched off, and one with it switched on, yields the absorp-

* A considerable literature exists on the subject. See for example a lengthy review paper by Vanasse and Sakai (1967).

FIGURE 1

Block diagram of experimental arrangement.

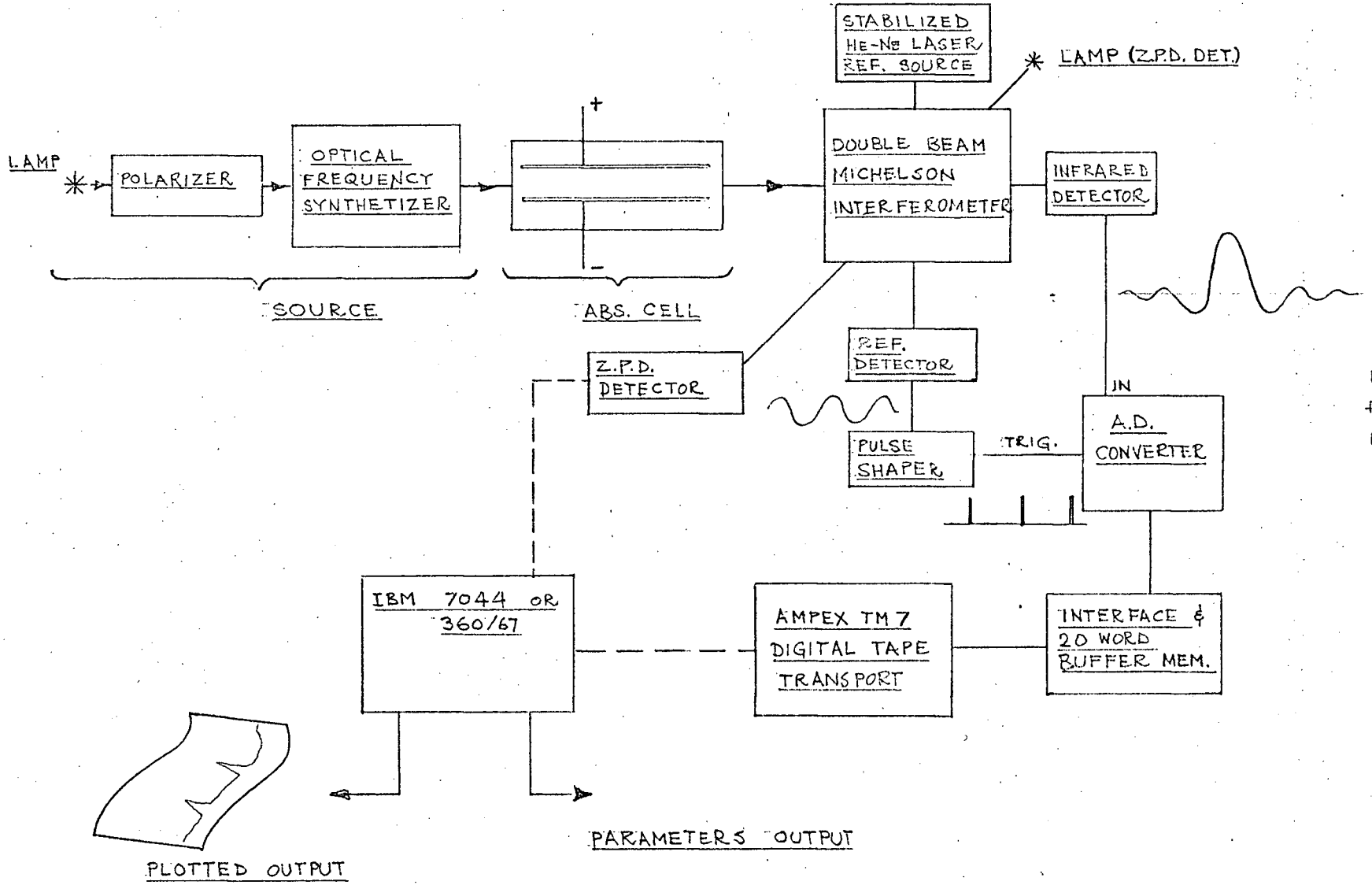
STABILIZED
HE-Ne LASER
REF. SOURCE
LAMP (Z.P.D. DET.)
LAMP
POLARIZER
OPTICAL
FREQUENCY
SYNTHETIZER
+
-
DOUBLE BEAM
MICHELSON
INTERFEROMETER
INFRARED
DETECTOR
SOURCE
ABS. CELL
Z.P.D.
DETECTOR
REF.
DETECTOR
IN
A.D.
CONVERTER
PULSE
SHAPER
TRIG.
IBM 7044 OR
360/67
AMPEX TM 7
DIGITAL TAPE
TRANSPORT
INTERFACE &
20 WORD
BUFFER MEM.
PLOTTED OUTPUT
PARAMETERS OUTPUT

tion coefficient in which we are interested. In what follows is a detailed description of the various parts of the apparatus, and the numerical analysis.

1.1 The absorption cell

In the course of the investigation three different absorption cells were employed. In each case the electric field was generated by applying a high voltage across two parallel plate electrodes bordering the light path.

In the first cell the absorption path was 100 cm long which provided adequate absorption over the pressure range from 4.5 atm. to 30 atm. at an applied field strength from 30 to 80 kV./cm. The cell is of the "light guide" type where two of the walls of the light guide are formed by the electrodes, separated by 3 mm (see Fig. 2a).

It was found that the use of copper electrodes allowed the application of relatively high electric fields without sparking even in the event that a spark had previously contaminated the electrode surface. As the pressure of the gas is reduced, the maximum allowable voltage that can be applied without causing sparking is reduced. Because the amount of absorption is proportional to the density and to the square of the applied field the usefulness of a cell of fixed length decreases rapidly towards lower pressure.

The second cell was also of the light guide type,

FIGURE 2a,b,c

Absorption cells.

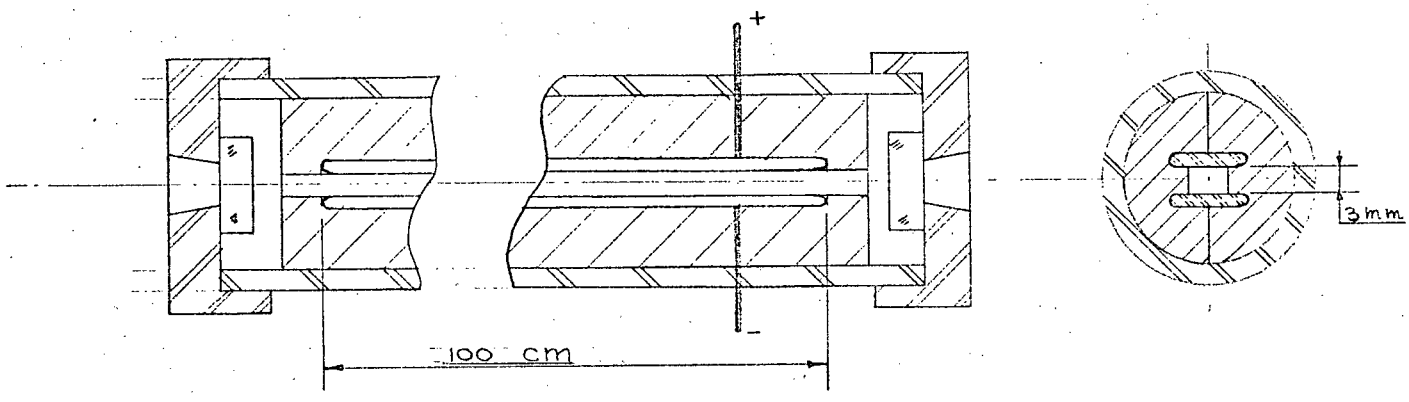
+
-
100 cm
3 mm

CELL A

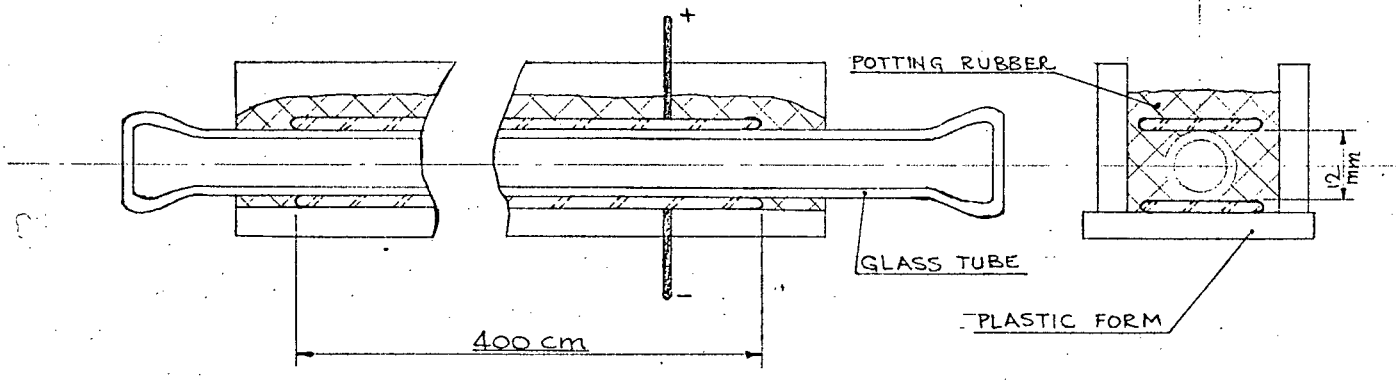
+
-
POTTING RUBBER
GLASS TUBE
PLASTIC FORM
400 cm
12 mm

CELL B

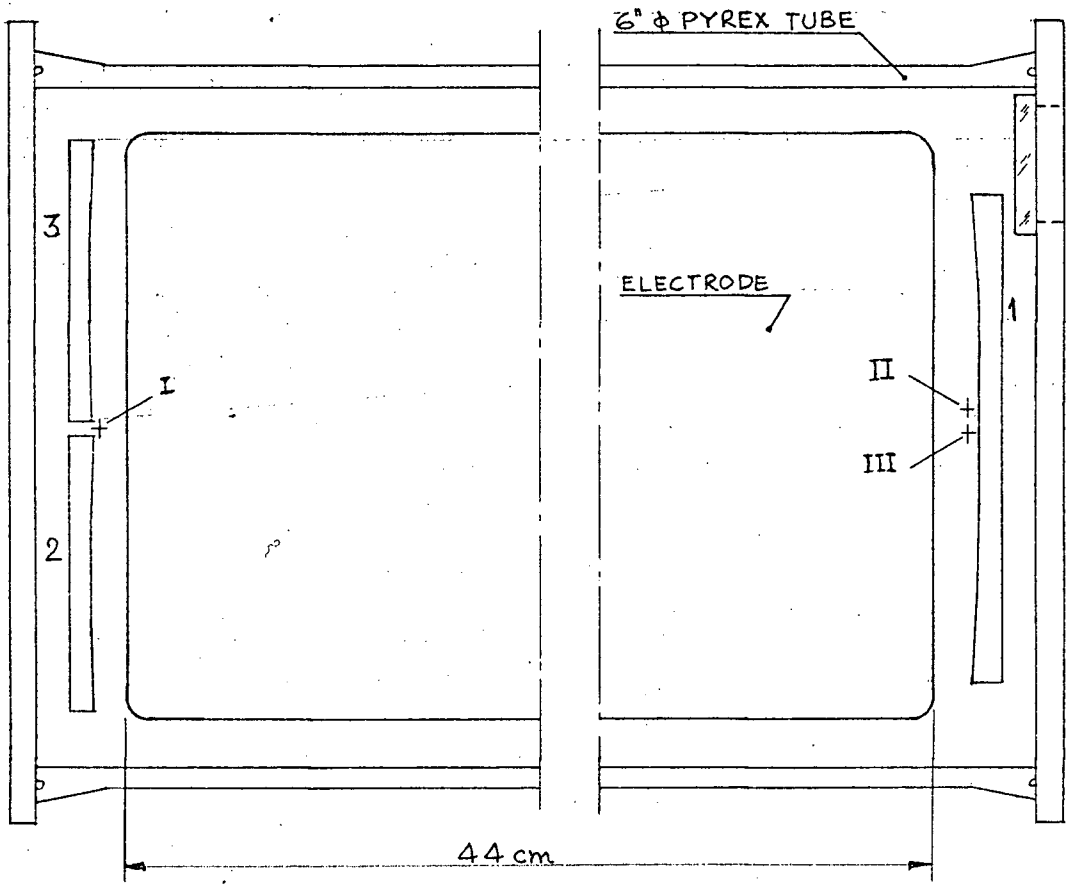

CELL C

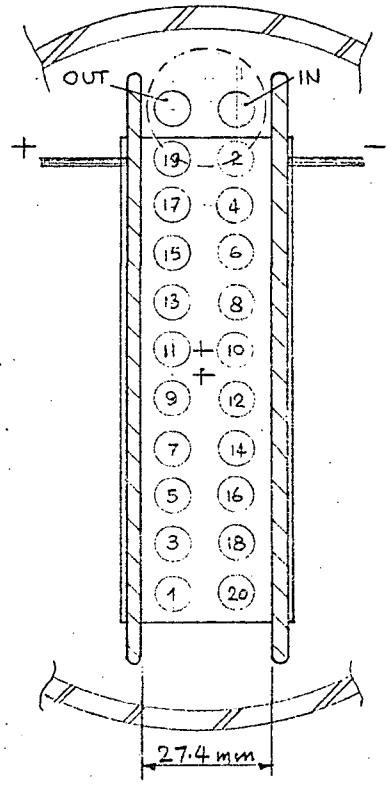

END VIEW SHOWING LOCATION OF IMAGES OF SOURCE ON MIRROR 3

but the electrodes were mounted on the outside of a glass tube so that sparking could not take place and hence a higher field strength could be maintained at lower pressures (see Fig. 2b). The electrodes were 400 cm long thus providing four times the absorption path of the first cell. In order to reduce light losses due to many reflections off the glass walls of the pressure vessel, the cross section was increased from 3 x 3 mm, as it was in the first cell, to 10 mm diameter. In this way the solid angle of the light cone entering the cell could be reduced while maintaining the same total incident flux of light. This cell provided adequate absorption spectra over the pressure range from 1.7 atm. to 4.5 atm.

The third cell used was a "multipass" or "White" cell. By means of three spherical mirrors, arranged at either end of an absorption cell as shown in Fig. 2c, the incident light can be made to traverse the space between the mirrors many times without loss of light due to the divergence of the incident beam. In order to retain a reasonably high field strength using existing high voltage power supplies, the electrodes were placed 2.5 cm apart and this fixed the maximum height of the mirrors. Mirrors 2 and 3 (see Fig. 2c) were 2.5 cm x 5.0 cm in size with a radius of curvature of 50 cm. With such small mirrors, to make the light gathering ability of the cell compatible with that of the interferometer, the images of the source formed at

mirror 1 should be at least 5 mm in diameter.

In Fig. 2c the position markings labelled with Roman numerals are the locations of the centers of curvature of the corresponding mirrors. Mirror 1 always images the surface of mirror 2 on mirror 3 and vice versa. Mirrors 2 and 3 transfer images of the entrance aperture (source) back and forth across the surface of mirror 1 until finally, after many transfers, the number of which is determined by the positions of centres II and III, the image spills off mirror 1 into the exit aperture as shown in section A-A of Fig. 2c. The maximum path attained with the multipass cell was 44 meters, using gold coated mirrors.

1.2 The Interferometer

The optical arrangement of this interferometer has been described in the literature previously (Buijs and Gush, 1967), but for the sake of completeness the schematic diagram of the optical path and a scale drawing of the mechanical arrangement have been repeated in Figs. 3 and 4 respectively. The optical path difference between the two separated beams is changed by displacing the two prisms parallel to the light path, the increase in path difference being four times the displacement. Small rotations of the prisms have no effect on the state of interference, which makes possible large displacements of the prisms without severe requirements on the precision of the slide ways.

FIGURE 3

Schematic diagram of optical path through Interferometer

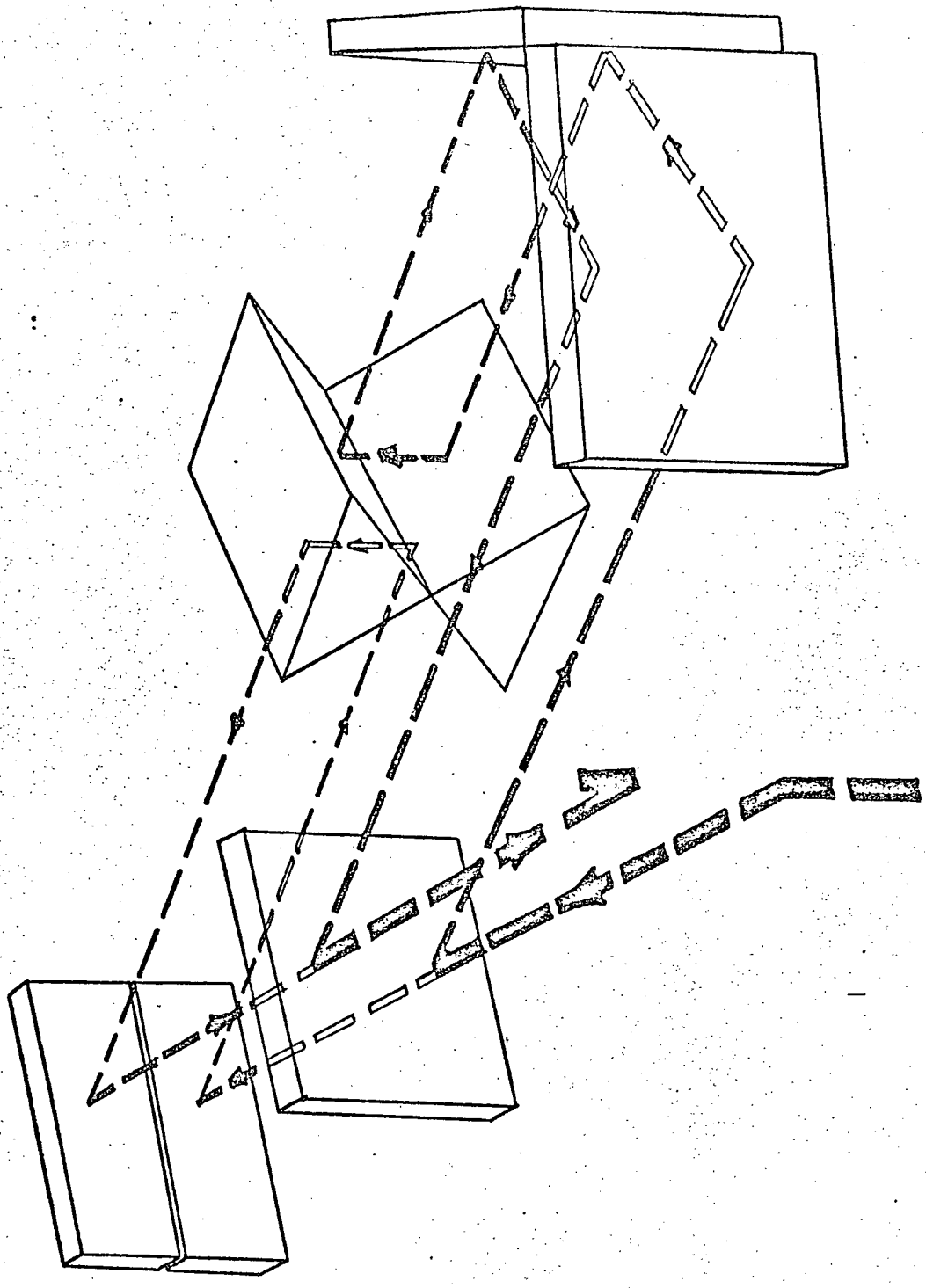

FIGURE 4

Scale drawing of mechanical arrangement of Interferometer

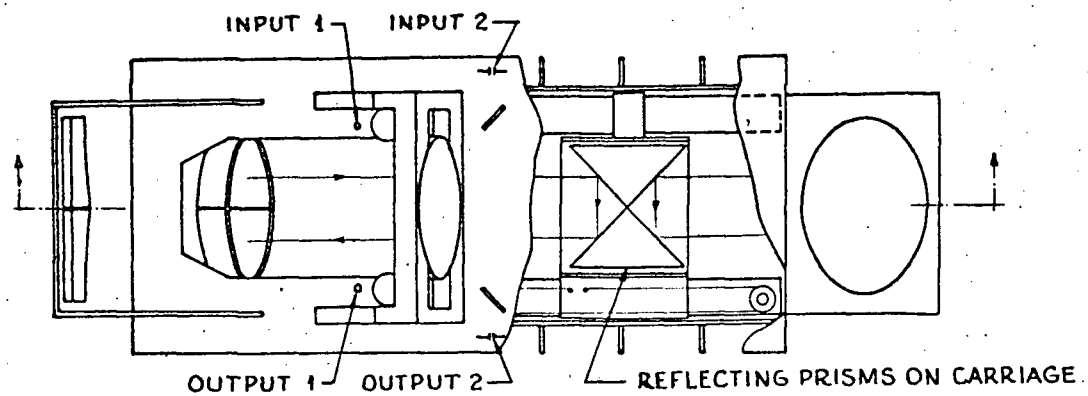
INPUT 1
INPUT 2
OUTPUT 1
OUTPUT 2
REFLECTING PRISMS ON CARRIAGE

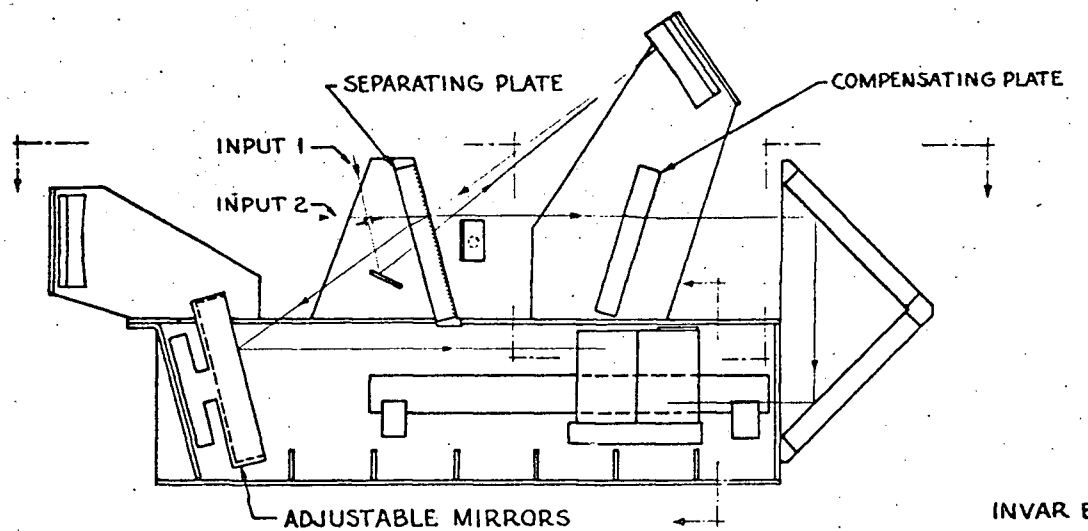
SEPARATING PLATE
COMPENSATING PLATE
INPUT 1
INPUT 2
ADJUSTABLE MIRRORS

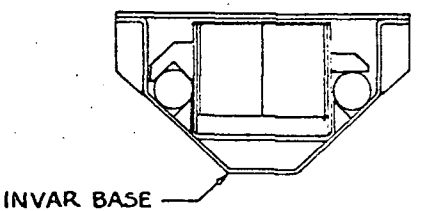
INVAR BASE

The instrument was designed to operate over a range of optical path difference from -4 cm to +103 cm. Two output beams are available for detection, and two input channels are available for sources. Each of the output and input beams is provided with an off axis paraboloid mirror of 50 cm focal length so that localized fringes may be formed at their focal planes. Appropriate diaphragms are placed in these focal planes in order to isolate that portion of the fringe pattern used for observation. The path difference in the interferometer is monitored by means of mono-chromatic fringes produced by the light of a highly stabilized single mode He-Ne laser. The fringes are converted to a train of pulses which command the A-D converter used to measure the infrared interferogram.

It is essential in the analysis to know accurately the zero path difference location of the infrared interferogram. If the spectral width of the bands of radiation under study is small, the zero path difference location is not obvious from the interferogram. It is thus necessary to illuminate the interferometer with an auxilliary white light source and detect white light fringes with a third detector placed off axis. The signal of this detector defines approximately the location of zero path difference. During a scan the path difference is varied continuously. The prism carriage is driven by a spring steel wire which is guided around pulleys at either end of the displacement path. One

of the pulleys is driven by a regulated d.c. motor through a set of reduction gears. The speed of the carriage was found to fluctuate by about $\pm$ 15% due to backlash in the various links from the motor to the carriage.

1.3 Detectors and signal conditioners

The interference fringes obtained from the radiation passing through the absorption cell and the interferometer are characterized by large swings in intensity near zero path difference, and very weak fringes on top of a large background flux of radiation away from z.p.d. It is imperative for the successful analysis of the information that the radiation intensity be converted linearly into an electrical signal, finally expressed in numerical form.

The most likely source of non-linearity was the detector, a lead sulphide cell. Two electrical circuits were tried as pre-amplifiers, shown in Figs. 5(a) and (b). In the former the detector is operated at constant current and performs as a voltage source, whereas in the latter the detector operates at constant voltage and is essentially a current source. Both circuits performed well for uncooled detectors, but for cooled detectors, only circuit 5 (b) gave adequately linear performance. The detectors were manufactured by Infrared Industries Inc. For room temperature operation the type B3 detector was chosen with an area of 1.5 x 1.5 mm^2, and for dry ice operation the type T1 was

used, of area 0.5 x 0.5 mm^2.

In the circuit shown in Fig. 5, the input operational amplifier is a high quality F.E.T.-input type having a very low input current noise, i_n, and low input voltage noise e_n. These sources of noise contribute to the output signal for circuit (a) as follows:

$$e_{out}\ (e_n) = e_n\ R_{det.}/R_{in}$$

$$e_{out}\ (i_n) = i_n\ R_{det.}$$

Input voltage noise can be controlled by choosing R_{in} sufficiently large, but input current noise cannot be controlled in this manner. In order to limit the noise output predominantly to detector generated noise, it was found necessary to pass a relatively high current through the detector by extending the bias voltage of the detector to beyond the output swing of the amplifier. This was accomplished by means of the insertion of a zener diode and current supply as shown in Fig. 5. Any noise signal created by the zener diode will, by virtue of the feedback, appear at the output of the operational amplifier, and only a portion equal to ($e_{nz}\ R_{det.}/AR_{in}$) will appear at the high voltage side of the detector (A is the open loop gain = 50000). For this reason the signal is taken from the high voltage side of the detector.

In circuit (b) the sources of noise contribute to

FIGURE 5

Schematic of detector electronics

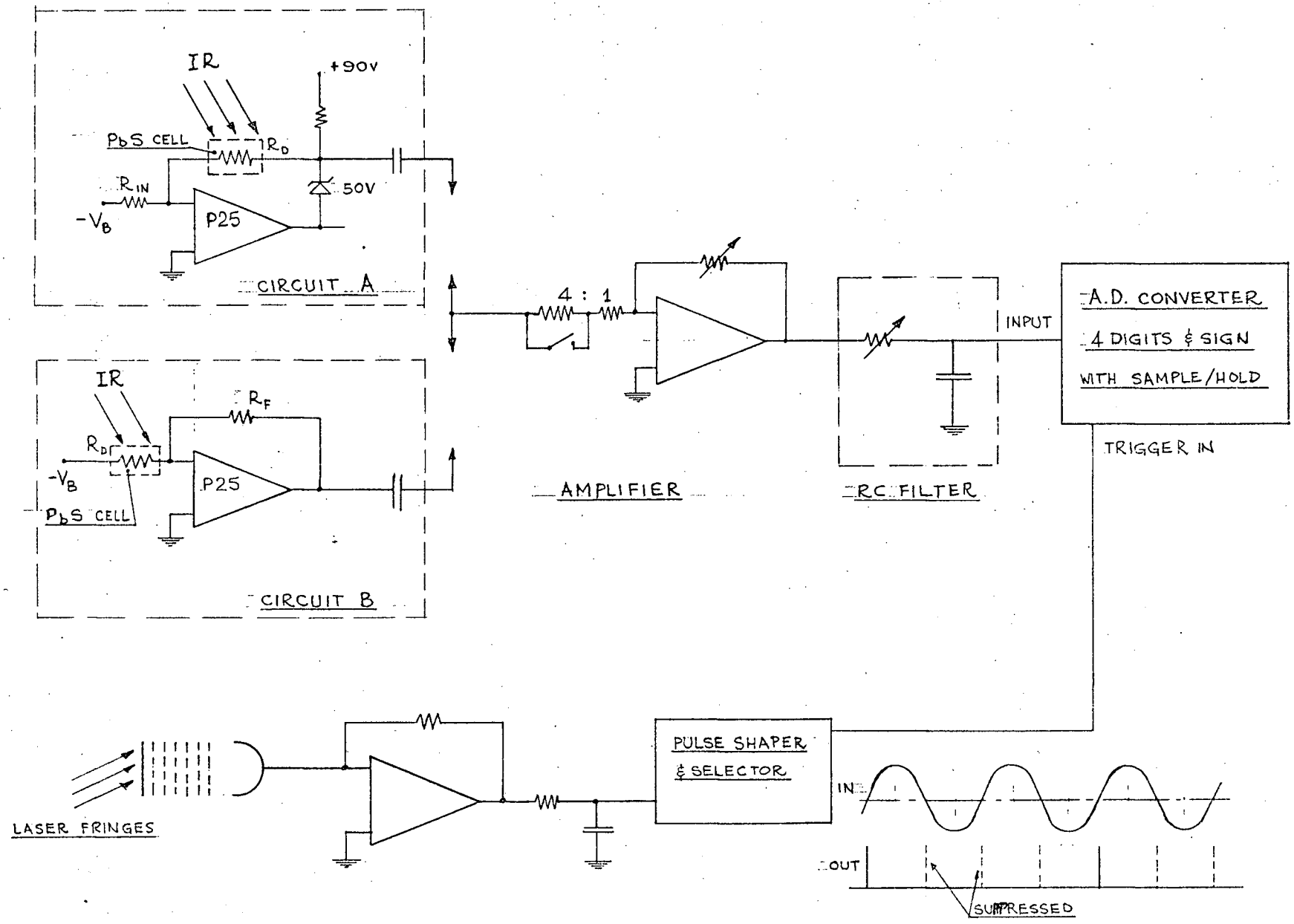
IR
+90V
PbS CELL
R_D
R_{IN}
50V
$-V_B$
P25
CIRCUIT A
IR
R_F
R_D
$-V_B$
P25
PbS CELL
CIRCUIT B
4 : 1
AMPLIFIER
RC FILTER
INPUT
A.D. CONVERTER
4 DIGITS & SIGN
WITH SAMPLE/HOLD
TRIGGER IN
LASER FRINGES
PULSE SHAPER
& SELECTOR
IN
OUT
SUPPRESSED

the output signal in a manner similar to that of circuit (a):

$$e_{out}\ (e_n) = e_n\ R_f/R_{det}.$$

$$e_{out}\ (i_n) = i_n\ R_f\ .$$

Again the ratio R_f/R_{det} is made small to reduce the effect of voltage noise and at the same time allow a high voltage across the detector without requiring an excessive voltage at the output of the amplifier.

For the same total flux of incident radiation it is well known that greater detectivity is obtained from a lead sulphide detector when the area is a minimum. For this reason the exit aperture defining the central fringe of the infrared interference pattern was imaged on the detector by a three element germanium condenser having a speed of f/1.o and a demagnification factor of 6. The condenser elements were anti-reflection coated for optimum transmission at $\lambda = 2.4\ \mu m$. The condenser also served automatically as a filter to reject radiation of wavelengths less than about $2\ \mu$.

It is customary when using a PbS cell to employ a chopper to interrupt the light signal periodically; the alternating signal from the cell is then synchronously demodulated to yield a voltage proportional to the light intensity. This was not necessary in these experiments because the interference fringe frequency during scanning

was typically about 35 sec^{-1} which falls in a frequency band where PbS detectors perform reasonably well. A simple amplifier was thus used after the preamplifier with a low frequency cut off in the range of ≤ 2 c.p.s. and a high frequency half power point at 70 c.p.s. (see Fig. 5). Phase shifts were kept to a minimum to avoid undesirable phase shifts in the interferogram introduced by fluctuations in the scanning speed.

When the electrical noise generated by the detector becomes comparable to the smallest increment of the A-D converter, the detector noise is no longer the determining factor in the signal to noise ratio of the spectrum. The resolution of our A-D converter is one part in 20000 of the full scale signal excursion. When used in conjunction with the two light guide absorption cells, the r.m.s. noise of the room temperature detector was about 1/5000 times the signal excursion at z.p.d. However, the amount of light transmitted through the White cell was about ten times less than through the light guide cells and hence a cooled detector with a smaller noise was used to improve the spectrum. Because of the considerable improvement in signal to noise ratio of the cooled detector it was found advantageous to increase the amplifier gain by a factor of 5 at a selected path difference so that the large fringes at z.p.d. will not saturate the A-D converter while at the same time a more accurate digital representation of the low level

signals is provided. The gain change is computationally restored, but the accuracy of the spectrum depends on the precision with which the gain change is known.

1.4 Source and Frequency synthetizer

In absorption spectroscopy, as the name implies, one studies the radiation absorbed from some continuum source by the sample under study. In case there are only a few narrow spectral lines, the total intensity absorbed is only some very small fraction of the incident intensity. This is troublesome in Fourier transform spectroscopy because the detector is "loaded" with a large signal coming from radiation in spectral regions between the lines under study, which is essentially of no interest. It is then necessary to restrict the spectrum of the continuous source to only those spectral regions in which absorption lines are being studied. Enough of the continuum must be left, naturally, to obtain precise line profiles, but apart from that one rejects as much of it as possible. In the present experiment this has been achieved with a "frequency synthetizer". To further increase the fraction of light absorbed a polarizer was employed to pick out that component which is maximally absorbed in the static field cell. However, even with all these precautions, in a typical case less than about 1.6×10^{-4} parts of the incident flux was absorbed by the hydrogen gas when the electric field was applied.

The radiation source was a small tungsten filament lamp operated at its maximum allowable temperature from a regulated d.c. supply ("Hanimex" projection lamp, 8 volts, 50 watts).

The polarizer, which immediately followed the source, was constructed as shown in Fig. 6, and operates by means of reflecting the radiation from a silicon slab at the Brewster angle. Due to the high index of refraction of silicon, the polarizer has an efficiency of about 80% over a wide spectral range.

The radiation is restricted to narrow bands centered at the various absorption frequencies by means of an optical frequency synthetizer which is shown schematically in Fig. 7. The instrument consists of a grating spectrometer in which the diffracted rays in the "exit plane" are selectively reflected back to the entrance slit by means of a mask and a set of small spherical mirrors.* The incoming and outgoing rays may be separated in front of the entrance slit with a beam splitter, but here it was more convenient to make an angular separation of the two light beams, using different parts of the grating for the incoming and outgoing rays. With a 600 ℓ/mm diffraction grating, 10 cm high x 13 cm wide, and an entrance aperture of 3 x 3 mm, the synthetizer has a

* Mirrors are spherical in order to image the collimator each on itself.

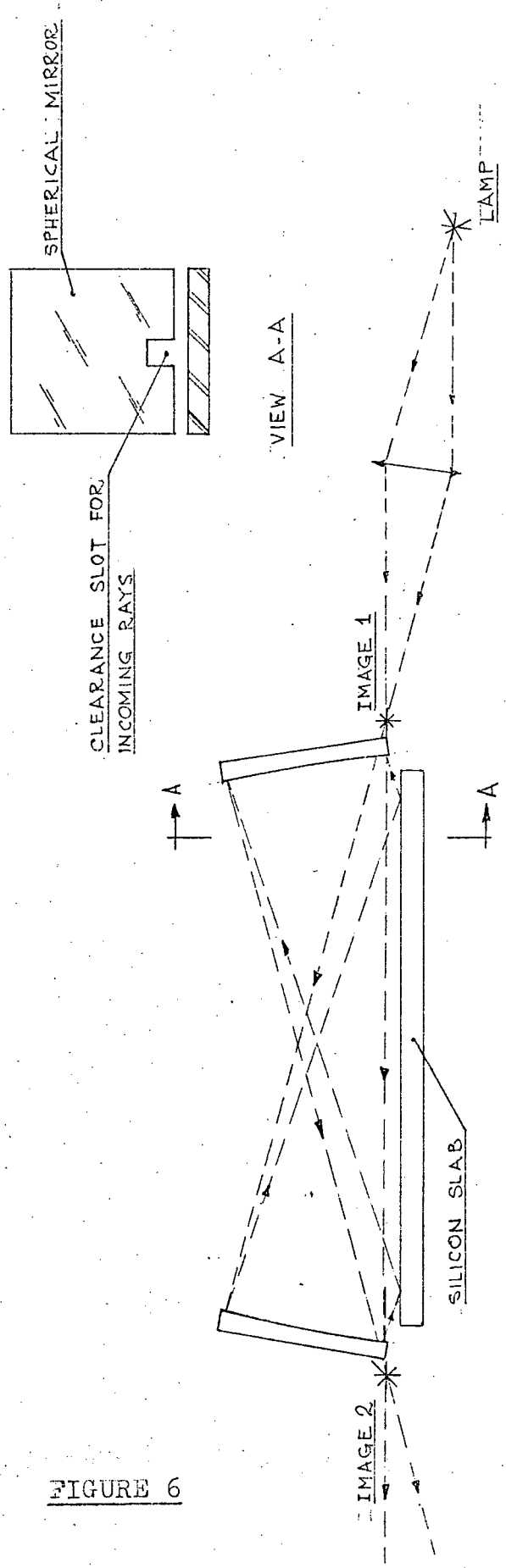

FIGURE 6

INFRARED POLARIZER

(APPROX. FULL SCALE)

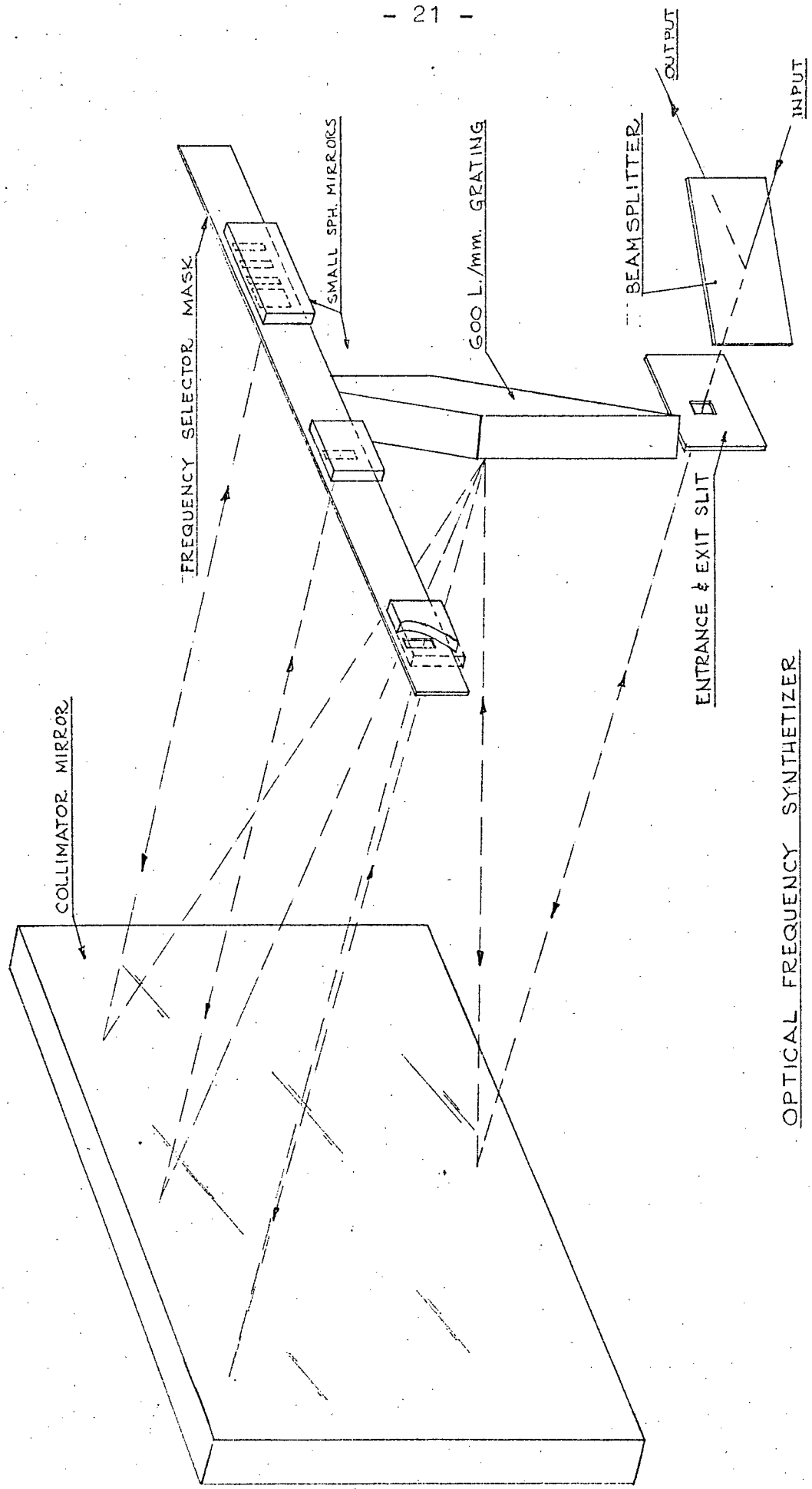
OUTPUT
INPUT
BEAMSPLITTER
SMALL SPH. MIRRORS
600 L./mm. GRATING
FREQUENCY SELECTOR MASK
ENTRANCE & EXIT SLIT
COLLIMATOR MIRROR
OPTICAL FREQUENCY SYNTHETIZER

FIGURE 7

light gathering power compatible with the interferometer. The actual spectral bands obtained with the instrument are shown in Fig. 8.

1.5 Data Collection

As we have already mentioned the infrared interferogram is measured at discrete points of optical path difference in order that a numerical Fourier transform may be carried out. The electrical signal from the detector is measured with an analog-digital converter which is triggered by pulses generated from the laser reference interferogram. The measurements of the A-D converter, or "words", are stored on magnetic tape, which can be read by a large high speed computer. We describe here this data acquisition system.

The analog to digital converter is an "Eeco" type 760-A having an output of four decimal digits and sign. The instrument can operate at an asynchronous rate of up to 30000 measurements per second, and has a built-in sample and hold unit with an aperture time of less than 1 μsec (aperture time equals the time required to look at signal for purpose of measurement). The settling time of the sample and hold unit, that is, the waiting period, after a large signal change has taken place, before an accurate measurement can be taken, is about 10 μsec. These properties allow the A-D converter to follow a full scale sinusoidal voltage of frequency ν with an accuracy of 1 part in 20000 for ν less

FIGURE 8

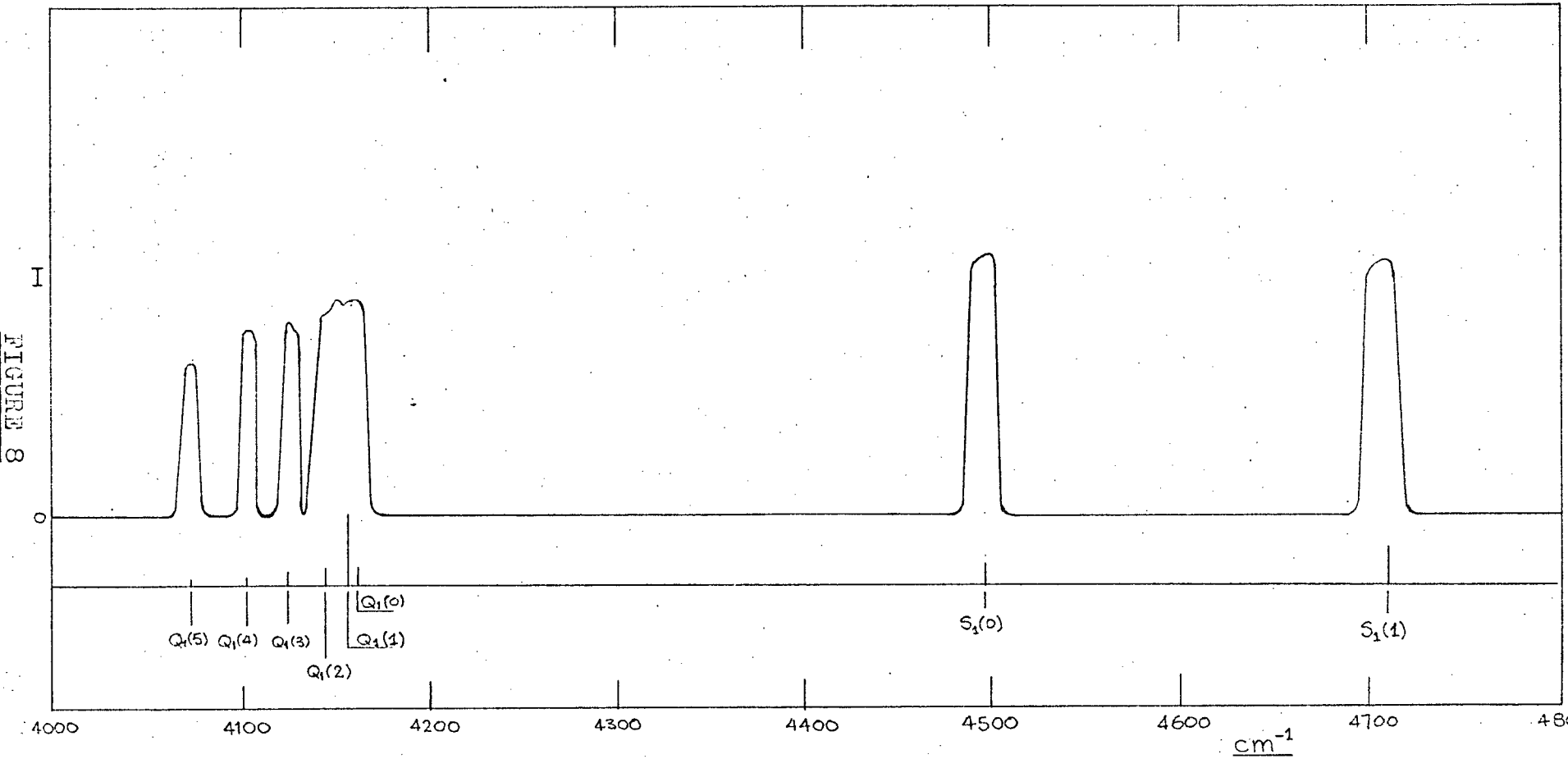

SPECTRAL CONTENT OF 'SOURCE'

SHOWING ALSO LOCATION OF ABSORPTION IN H_2

than about 150 sec^{-1}. In conjunction with the trigger pulses derived from selected crossovers of the laser fringes, and the fast sample and hold unit, digital measurements can be obtained at precisely known values of path difference despite scanning speed fluctuations.

The digital information is recorded on magnetic tape in a form suitable for further processing in a large digital computer. The tape-transport is an Ampex model TM7211 which is coupled to the A-D converter via a buffer memory and control logic unit. The control logic unit contains all the functions required to generate I.B.M. compatible tape.

The buffer memory, constructed by the author, consists of 2 chains of integrated circuit "shift registers": one, 4 bits wide by 80 bits long which can store 80 binary coded decimal (B.C.D.) digits, and the other 1 bit wide by 20 bits long to hold 20 sign bits. The output of the A-D converter appears simultaneously on 17 output wires; 16 wires for the four, four bit digits, and the 17th for the sign. As each measurement is taken, the four digits are "pushed into" the shift register sequentially while all existing information is moved up 4 positions, and the sign is pushed into its register. When the shift registers are full, (after 20 measurements) the tape-transport is started and the content of the registers is quickly "pushed out" onto tape. There are two modes of operation providing two speed ranges for

the rate of taking measurements:

1) the tape transport is turned on after the 20th measurement, in which case it is not possible to enter a new measurement into the register for 15 ms. after the 20th measurement has been entered (5 ms. for data transfer to tape, and 10 ms. start time of transport). Considering that the A-D converter can keep one measurement at its output until a new measurement is taken, the time between two measurements must be greater than 7.5 ms. giving a range of from 0 - 130 measurements/sec.

2) the tape transport is turned on after the 19th measurement: In this case the 20th measurement must occur within 10 ms. of the 19th, and the time between measurements cannot be less than 5 ms. thus giving a range of from 100 - 200 measurements/sec.

By virtue of the size of the buffer memory, "physical tape records" are 20 measurements (words) long occupying about 0.1" of tape. The stopping and starting between records requires 0.75" of tape. Thus every record of 20 words requires 0.85" so that a reel of 2400' holds about 678000 measurements. A 3600' reel holds a maximum of 10^6 words. If a record is "unreadable" during later processing, only 20 words of information are lost (and are later replaced by zeros to retain the phases of subsequent information); this compensates somewhat for the inefficient use of tape. The digital recording system was planned to operate at

a reliability level sufficiently high to be able to record interferograms of 10^6 measurements with only a small probability of error. In retrospect, there has never been a visible indication of an error, not even the loss of information due to unreadable records.*

1.6 Data Analysis

Once an interferogram has been recorded in digital form one proceeds to the Fourier Analysis. If the interferogram is a symmetric function of the path difference (this is assumed in our analysis, and confirmed by measurement) the spectrum can be obtained by a cosine transform only, starting the integration at zero path difference, and proceeding to the maximum path difference. The zero path difference point must be located to within a small fraction of the shortest wavelength contained in the spectrum, otherwise the spectral lines will not be symmetric. The procedure to find z.p.d. is outlined below.

A second procedure to be carried out is the reduction of the number of samples on the interferogram to the minimum value consistent with the width of the spectrum studied. In our procedure more points are actually measured than is absolutely necessary to define the spectrum. The

* except for one occasion during which, for good reason, the parity generator of the digital tape transport failed, and an experiment had to be rerun.

number of points is reduced by a numerical filtering procedure which has been designed especially to fit the hydrogen spectrum. In Fig. 9 is shown a block diagram indicating the various steps in the data analysis.

The connection between the interferogram and the spectrum is through a Fourier Integral:

$$B(\sigma) = \int_{-L}^{L} I(\delta)\cos(2\pi\sigma\delta)\,d\delta$$

where $I(\delta)$ is the intensity as a function of path difference δ, and σ is the frequency in waves per cm. When the interferogram is not measured continuously, but is sampled at discrete points, equally separated, the integral above is replaced by a sum:

$$B(\sigma)' = \sum_{n=-N}^{N} h\, I(nh)\cos(2\pi\sigma nh)$$

The spectrum $B(\sigma)'$ is represented by a Fourier series, and is hence periodic of period $\sigma = 1/h$. The true spectrum $B(\sigma)$ and the periodic spectrum $B(\sigma)'$ will coincide in a certain domain of the frequency axis only if the interval h is sufficiently small, and if $B(\sigma)$ is non zero only in either one finite domain, or in a finite number of finite domains. The total number of points N required to represent the spectrum is then markedly dependent on the actual form of $B(\sigma)$. Because the hydrogen lines lie in distinct regions of the spectrum it has been possible to reduce the number of points required on the interferogram below that usually stated

FIGURE 9

Block diagram of data analysis procedure

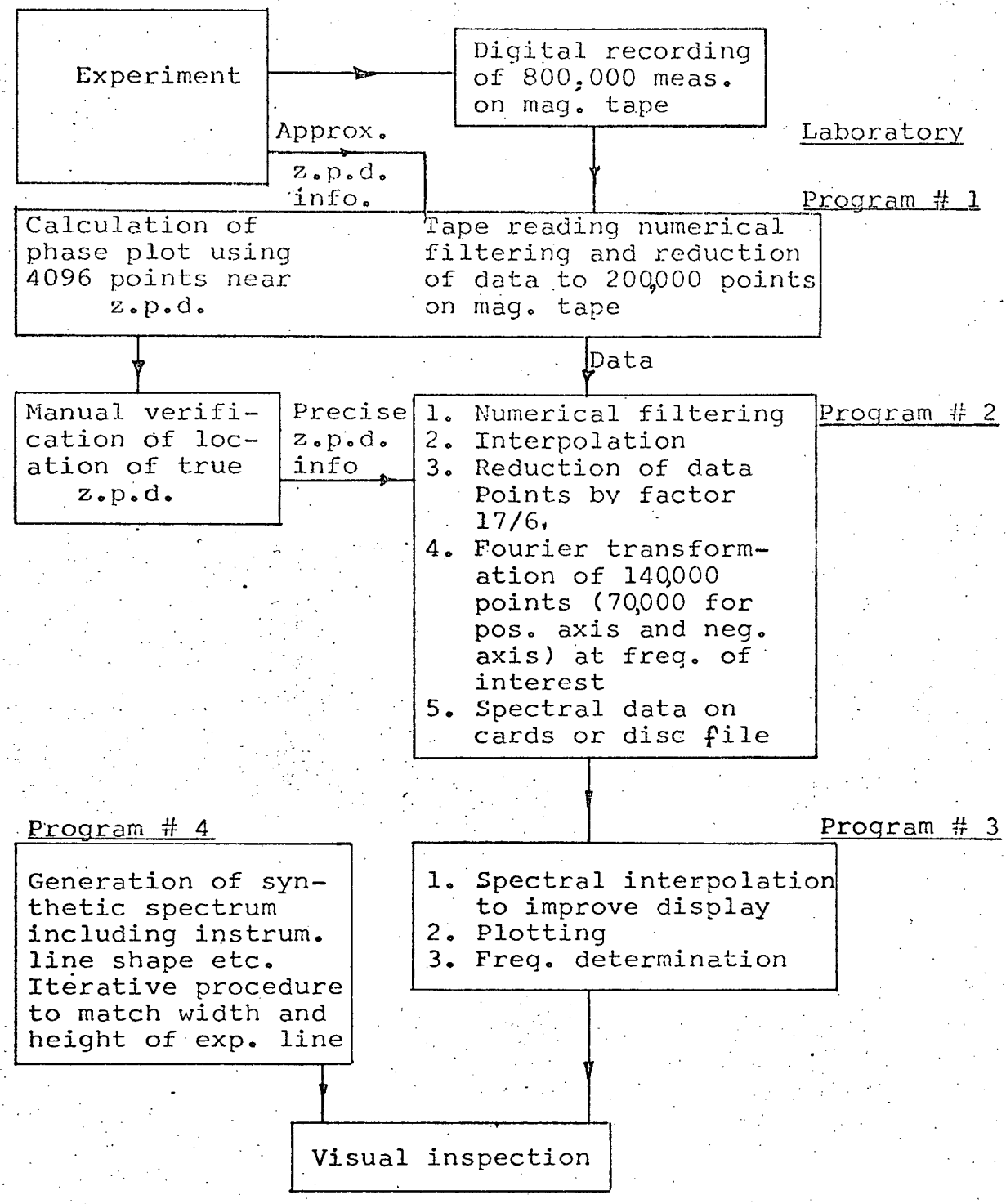
Experiment
Digital recording of 800,000 meas. on mag. tape
Approx. z.p.d. info.
Laboratory
Program # 1
Calculation of phase plot using 4096 points near z.p.d.
Tape reading numerical filtering and reduction of data to 200,000 points on mag. tape
Data
Manual verification of location of true z.p.d.
Precise z.p.d. info
1. Numerical filtering
2. Interpolation
3. Reduction of data Points by factor 17/6,
4. Fourier transformation of 140,000 points (70,000 for pos. axis and neg. axis) at freq. of interest
5. Spectral data on cards or disc file
Program # 2
Program # 4
Generation of synthetic spectrum including instrum. line shape etc. Iterative procedure to match width and height of exp. line
Program # 3
1. Spectral interpolation to improve display
2. Plotting
3. Freq. determination
Visual inspection

FIGURE 9

in the sampling theorem: $h \leq 1/2\,\sigma_{max}$, σ_{max} being the highest frequency in the spectrum. This procedure is outlined below.

The spectral content of the analog signal is shown in Fig. 10a, where the actual spectrum of the infrared source is shown along with the r.m.s. noise spectrum generated by the detector and electronics (the latter has also been drawn on a wave number scale, obtained by multiplying the electrical frequency by a suitable coefficient depending on the velocity of the moving mirror). The r.m.s. noise spectrum is assumed to be positive and the infrared source spectrum is symmetric by virtue of the fact that the interferogram is assumed symmetric about its origin. The spectrum for a sampled interferogram is shown in Fig. 10b; the repetitions of the spectra are called aliases. According to Fig. 10a, a sample frequency of about 20000 cm^{-1} would completely avoid overlapping of aliases. However, by selecting a sample frequency of 7901.54 cm^{-1}, which corresponds to one sample per two complete laser fringes, the noise in a band from 3000 to 3950.72 cm^{-1} becomes added to the region from 3950.72 cm^{-1} to about 4900 cm^{-1}, which covers the region of interest. Thus by allowing a deterioration of signal to noise ratio in going from analog to digital information by a factor of $\sqrt{2}$ (incoherent addition of two equal noise components) a saving of a factor of 2½ is obtained in the number of measurements required. At this sample frequency 800,000 data points represent an interferogram of 100 cm path difference.

FIGURE 10

Spectral distributions arising during various steps of the analysis

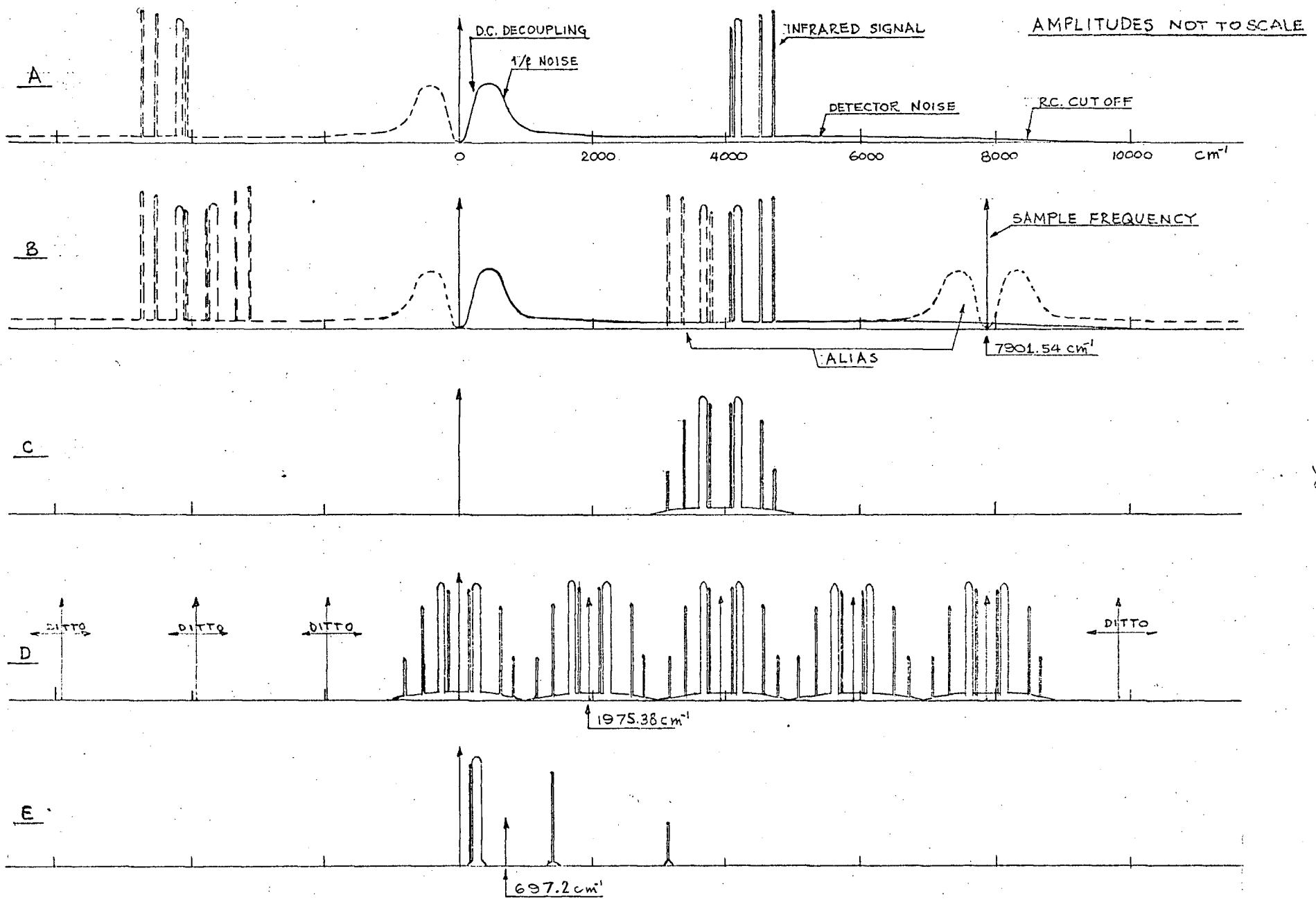
AMPLITUDES NOT TO SCALE
A
D.C. DECOUPLING
1/f NOISE
INFRARED SIGNAL
DETECTOR NOISE
R.C. CUT OFF
0
2000
4000
6000
8000
10000
cm⁻¹
B
SAMPLE FREQUENCY
ALIAS
7901.54 cm⁻¹
C
D
DITTO
DITTO
DITTO
DITTO
1975.38 cm⁻¹
E
697.2 cm⁻¹

In order to reduce the above number of data points prior to Fourier transformation without further deterioration of the signal to noise ratio, the noise band outside the region of interest (see Fig. 10b) is removed by means of a numerical filtering operation performed while the data is being read by the computer. Because of the large quantity of data involved, the "pulse response" function of the filter band must be represented by as few data points as possible so that the numerical filtering operation will consist of very few operations per input point. By using a Gaussian band pass filter function and by not attempting to interpolate the data points to include the zero path difference point in this filtering operation, it was possible to reduce the number of operations (essentially one multiplication and two additions per operation) to four per input point. The resulting interferogram has a frequency content as shown in Fig. 10(c) and can now be sampled at a frequency of 1975 cm^{-1} (one quarter the previous sample frequency) without overlapping of aliases. Thus in the initial numerical filtering operation the number of measurements is reduced from 800,000 points to 200,000 having a spectral content as shown in Fig. 10(d). These 200,000 points are stored on magnetic tape in a highly compressed form. This tape is kept for future reference, while the laboratory generated tape is reused.

About 4000 measurements are made along a typical interferogram before z.p.d. occurs. Using some of these

measurements along with about an equal number after z.p.d., a low resolution spectrum is calculated using Fourier cosine and sine transformations and using the measurement singled out by the white light fringes as the assumed center of the interferogram. Then by calculating the phase angle* $\left(\phi = \tan^{-1}\left[A_{sin}/A_{cos} \right] \right)$ associated with spectral amplitudes at different frequencies it is possible to find the distance in path difference of the assumed center of the interferogram to the true center ($\Delta = \frac{\phi \lambda}{2\pi}$). In this way it is possible to locate z.p.d. to within $\pm$ 0.3% of a sample interval.

In a second computer program, a new interferogram is calculated from the intermediate interferogram (represented by 200000 data points) by means of another numerical filtering operation. In this case, however, the pulse response of the filter function is calculated at such phases so that the first point in the new filtered interferogram occurs exactly at z.p.d. During this filter operation more regions in the spectrum are set to zero allowing still closer aliasing and consequently a further reduction in the number of required sample points.

* ϕ is determined to within a multiple of 2π, but by drawing a straight line through a plot of ϕ v.s. frequency the absolute value of ϕ is obtained from the fact that $\phi = 0$ at zero frequency. Dispersion would cause a non-linear relationship between ϕ and freq. making the above procedure difficult.

It is possible to calculate the pulse response of a multiband narrow band filter where the bands of the filter are chosen amongst the various aliases as indicated in Fig. 10d. Then the spectral content of the new interferogram after calculating very many samples would be as indicated in Fig. 10e. We now sample this interferogram in such a way that the different bands occur in a completely different set of aliases. Then the "principal alias" (near origin of frequency scale) is made to lock as in Fig. 11. The spectral information has not been compromised in this final interferogram, but the frequencies of the different parts are no longer simply related; nevertheless an exact relationship still exists. The data reduction factor thus obtained is 17/6 which means that the pulse response must consist of six sets of numbers each with different phases.

By considering that the Fourier cosine transform is the same as the real part of a complex Fourier transformation carried out on a real function, it is possible to apply the extremely fast method of complex Fourier transformation developed by Cooley and Tukey (1965). This method of complex Fourier transformation has been extended to large arrays of data by means of a factoring technique developed by the author (Buijs, 1969). By means of this factoring technique the spectrum is calculated in blocks. This blocking procedure has the advantage that blocks containing no spectral information of interest need not be calculated,

FIGURE 11

Spectral distribution before Fourier transformation

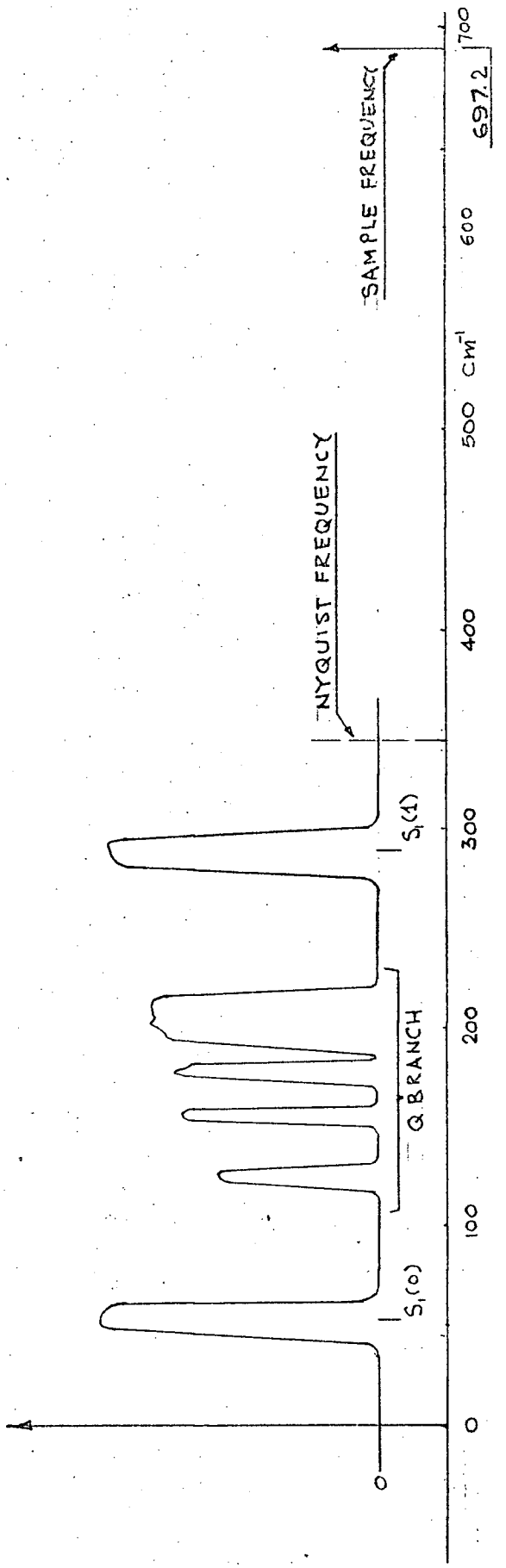
SAMPLE FREQUENCY
697.2
NYQUIST FREQUENCY
S₁(1)
Q BRANCH
S₁(0)
0
100
200
300
400
500 CM⁻¹
600
700

which is not the case with the original program of C. and T.

In the Fourier transformation, spectral amplitudes are calculated at frequency intervals equal to $\frac{1}{2}L$ cm^{-1} where L is the length of the single ended interferogram in cms. This spacing is only slightly less than the limit of resolution, and the representation of a very sharp line in the spectrum is just a point. In order to improve the spectral representation for display purposes, the spectral data is convolved with an analytically calculated replica of the instrumental line shape function and the final spectrum is calculated at four times as many frequencies as the original one. At this point the logarithm of the ratio of background intensity to spectrum intensity is plotted on a "Calcomp" plotter above a calibrated frequency scale. The frequency scale on the graph corresponds to 1 cm^{-1} ≡ 18" (for 0.0055 cm^{-1} res.). In the work here, the spectral lines being narrow, only a fraction of a wave number near each absorption line of hydrogen is plotted.

Because of the complexity of the above analysis, it may be interesting to compare the numbers of computations involved in the above analysis with a few simpler alternatives:

1) Straight complex Fourier transformation of a double ended interferogram consisting of 1.6×10^6 data points:

$98 \times 8192 \times 14 \times 2 = 22.6 \times 10^6$ (blocks of T.& C. transforms)
$6 \times 2000 \times 196 \times 2 = 4.7 \times 10^6$ (spectral assembly)
total $= 27.3 \times 10^6$ calculations

(this alternative would require double the quantity of input data).

2) Numerical filtering reduction of data and interpolation to obtain a symmetric interferogram with known center:

$70000 \times 116 = 8.1 \times 10^6$ (numerical filtering)
$18 \times 8192 \times 14 \times 2 = 4.1 \times 10^6$ (blocks of T.& C. transforms)
$6 \times 2000 \times 36 = .4 \times 10^6$ (spectral assembly)
total $= 12.6 \times 10^6$ calculations

3) Analysis as described above:

$200000 \times 20 = 4.0 \times 10^6$ (1st filtering)
$70000 \times 29 = 2.0 \times 10^6$ (2nd filtering)
$18 \times 8192 \times 14 \times 2 = 4.1 \times 10^6$ (blocks of T.& C. transforms)
$6 \times 2000 \times 36 = .4 \times 10^6$ (spectral assembly)
total $= 10.5 \times 10^6$ calculations.

One "calculation" in the above comparison consists roughly of one multiplication and several additions and index changes. The often time consuming auxiliary calculations (such as evaluation of cosine functions) and data transfer operations have been completely ignored in the above comparison.

Most recently, spectra have been obtained using the new I.B.M. 360/67 computer installation in the University of B.C. computation center. Since this is a time sharing

installation, computation tasks are evaluated in "computer dollars" based on an hourly rate schedule for each of the different aspects of the installation used. Program # 1 (see Fig. 9) costs about C$ 30.00 at a priority level of 0.9 (the cost is reduced by a factor as the priority required of the task is reduced) using a very fast machine language tape reading subroutine. Program # 2 costs about C$ 54.00 at the same priority level. Priority levels of 0.4 or 0.6 are commonly used. These are the costs, per spectrum.

1.6 Reliability of frequencies

Provided that the interferogram is sampled at regular intervals, the spectrum resulting from a digital Fourier transformation of this data will lie on a frequency scale that is highly linear. Hence the spectrum is completely calibrated when one frequency is known. The sample rate (frequency) in this experiment is derived from the fringes produced by a highly stabilized He-Ne laser, and the latter becomes the frequency standard. The precision with which the absolute value of the mean sample frequency can be established depends on the accuracy with which the central frequency of the laser line is known, on the knowledge of the direction of the light passing through the interferometer, and finally, since the interferometer was operated in air, on the refractive index of air.

Irregularities in the sample interval arise from

noise in the reference fringe signal and from electrical phase shifts due to mirror speed fluctuations. These fluctuations are believed to be random and statistically independent from one sample to another. Then after taking N measurements of path difference during which the magnitude increases linearly, the accumulated measurement of path difference will be

$$\bar{L} = \sum_{n=1}^{N} nh$$ where h is the sample interval.

For each of the N measurements the r.m.s. deviation is assumed to be the same (say ϵ) then the r.m.s. deviation in $\bar{L}$ is

$$\sqrt{\overline{\Delta\epsilon^2}} = \sqrt{\sum_{1}^{N} \epsilon^2} = \sqrt{N}\,\epsilon$$

and the fractional r.m.s. deviation will be

$$\frac{\epsilon\sqrt{N}}{\bar{L}} = \epsilon\sqrt{N}/h\left(N^2/2 + N/2\right) \simeq 2\epsilon/hN\sqrt{N}\ ^{*}$$

Typically $\epsilon/h \leq .1$ so that the uncertainty in the mean sample frequency due to random variations in individual measurements is about 6×10^{-10} for an interferogram consisting of 5×10^{5} measurements. An additional effect of sample irregularities would be to reduce the signal to noise ratio of the spectrum particularly at 1st overtone frequencies of strong features.

The laser is a "Spectra Physics" type 119 He-Ne C.W. laser having a highly stabilized tunable cavity, but without

* This is analogous to finding the error in the slope of the best straight line which goes through a number of points.

the λ servo option. Using a monitoring system suggested for checking out the λ servo operation, it was found easy to maintain the frequency of the laser output to within $\pm$ 15 Mc (particularly in the later work, after gaining experience) of the transition frequency of the Ne^{20} line, with only infrequent manual adjustments. The frequency of the laser radiation was taken as $\sigma = 15798.0012 \pm .0005$ cm^{-1} in vacuum, (see Mielenz et al (1965), Engelhard (1966) and Mielenz et al (1968)).

The circular aperture limiting the extent of the infrared light passing through the focal plane of the collimator, and the point image of the laser light in the same focal plane must be concentric with each other and with the fringe pattern in order to specify the sample interval precisely in terms of the wave length of the reference laser. When this is the case, the average optical path difference experienced by the infrared rays will be

$$\bar{\delta} = n \lambda \left(1 - \frac{1}{4} \frac{r_m^2}{f_c^2}\right)$$

where $n\lambda$ represents the observed path difference in terms of a number of laser fringes times the wavelength, r_m is the radius of the aperture and f_c is the focal length of the collimator. Due to the smallness of the dimensions, the above alignment can be carried out with only limited precision and frequently the center of the fringe pattern may shift as a function of path difference.

Looking into the interferometer from the exit side one observes two coherent images of the source as seen through the two arms of the interferometer. If these images superimpose exactly at zero path difference, then the center of the fringe pattern will be stationary and in the direction of mirror motion. If the interferometer is "poorly adjusted" the two images will never superimpose, but "zero path difference" will occur when the images are side by side with respect to the direction of observation, and the fringe center would occur in a direction 90^{o} away from the direction of observation. The distance of closest approach (a) of the two images is obtained from the separation of adjacent fringes in the focal plane of the collimator. In this interferometer "a" can be reduced by means of adjustment of the mirrors to about 30 μ without difficulty. The path difference at the center of the infrared aperture in case of misalignment of laser image and aperture is

$$\delta = \frac{n\lambda \cos\theta_I}{\cos\theta_L}$$

where θ_I is the angle between the center of the infrared aperture and the fringe center and θ_L is the angle between laser image and fringe center. Now let $\Delta = (\theta_I - \theta_L)_{\text{LATITUDE}}$ (i.e. Δ is the angular difference between the infrared aperture and laser image measured towards the fringe center) then:

$$\delta = n\lambda \frac{\cos\theta_L \cos\Delta - \sin\theta_L \sin\Delta}{\cos\theta_L}$$

$$\cong n\lambda \left(1 - \tfrac{1}{2}\Delta^2 - \Delta \tan\theta_L\right), \text{but } \tan\theta_L = a/n\lambda$$

and $$\delta \cong n\lambda\left(1 - \tfrac{1}{2}\Delta^2\right) - a\Delta$$

It can be seen that aperture misalignment causes a fractional change in path difference and a "constant" shift in value. However, since Δ is measured in the direction towards the fringe center, the movement of this center may cause an unpredictable variation in Δ as a function of path difference and hence both terms must be considered as uncertainties in the average value of the sample interval. The maximum value of Δ can be estimated from the relative positions of the aperture center and the laser image and the most severe variation in Δ during a scan would be reversal of sign. Thus,

$$\delta = n\lambda\left(1 \overset{+\,0}{-\,\frac{1}{2}\Delta_m^2} \pm \frac{a\Delta_m}{\delta_{max.}}\right)$$

By displaying a projection of the aperture and the laser image, magnified about twenty times, it was possible in most cases to align their centers to within 0.2 mm (this alignment also improved with experience). For $\Delta_m = 4 \times 10^{-4}$ and $\delta_{max} = 70$ cm $\quad \delta = n\lambda(1 - 4 \times 10^{-8} \pm 5.7 \times 10^{-8})$

hence $$\bar{\delta} = n\lambda\left(1 - \frac{r_m^2}{4f_c^2} - 4 \times 10^{-8}\right) \pm 5.7\, n\lambda \times 10^{-8}$$

All experiments were carried out with the interferometer surrounded by the laboratory atmosphere, the exact temperature pressure and composition of which was not known during the experiment. For precise frequency calibration to vacuum wavenumbers, the index of refraction of air must be known at the laser frequency and in the infrared. The absolute value of the sample interval in cms. is equal to two times the wavelength of the laser light measured in the prevailing atmosphere plus aperture corrections;

$$h = \frac{2\,\lambda_{vac.L.}}{n_L}\left(1 - \frac{1}{4}\,\frac{r_m^2}{f_c^2} - 4 \times 10^{-8}\right)$$

The frequency in air of an infrared line, a relative distance d along the frequency axis will be;

$$\sigma_{IR} = \frac{d}{h} = \frac{n_L\, d}{2\,\lambda'_{vac.L.}}$$

where $\lambda'_{vac.L.} = \lambda_{vac.L.}\left(1 - \frac{1}{4}\,\frac{r_m^2}{f_c^2} - 4 \times 10^{-8}\right)$

then $\sigma_{IR\ vac.} = \frac{\sigma_{IR}}{n_{IR}} - \frac{n_L\, d}{2\,\lambda'_{vac.L.}\, n_{IR}}$

working in terms of the refractivity $S = n - 1$;

$$\sigma_{IR\ vac.} = \frac{d}{2\,\lambda'_{vac.L.}}\,(S_L + 1)\,(1 - S_{IR} + S_{IR}^2)$$

In evaluating this product, $S_L\, S_{IR}$ very nearly cancels with S_{IR}^2 so that $\sigma_{IR\ vac.} = \frac{d}{2\,\lambda'_{vac.L.}}\,(1 + S_L - S_{IR})$ is a good approximation up to third order in S.

According to Edlen (1966), effects of temperature and pressure on the index of refraction of air are highly wavelength independent so that these variations may be applied directly to the difference $(S_L - S_{IR})$. Variations in the composition of air are somewhat wavelength dependent and must be computed for S_L and S_{IR} separately.

$S_L - S_{IR}$ is directly proportional to pressure with the proportionality constant given by the conditions in standard air. Hence $(S_L - S_{IR})_p = (S_L - S_{IR})_s \times 0.001388\ p$ where p is in torr. For $p = 760 \pm 40$ torr and $(S_L - S_{IR})_s = 364.5 \times 10^{-8}$, the variation with pressure in $\sigma_{IR\ vac.}$ will be

$$\sigma_{IR\ vac.} = (\sigma_{IR\ vac.})_s\ (1 \pm 19 \times 10^{-8})$$

The temperature variation of the refractivity of air is given by $(S_L - S_{IR})_t = (S_L - S_{IR})_s \times (1 + .00367t)^{-1}$ where t is in $^{\circ}C$. The temperature in the laboratory was found to be $21.5^{\circ}C \pm 1.5^{\circ}C$. Then the variation of $_{IR\ vac.}$ with temperature will be

$$\sigma_{IRvac} = (\sigma_{IRvac})_s \times (1 \pm 2 \times 10^{-8})$$

The saturated water vapour pressure in air at $21^{\circ}C$ is about 18.6 torr (Clark's tables (1957)). Therefore extreme changes in relative humidity could cause a variation of 18 torr in the partial pressure of water vapour in the air. A formula for the difference in refractivity of moist air and dry air is given by Edlen (1966) as:

$$(n_f - n) = -f\ (5.722 - 0.0457\sigma^2) \times 10^{-8}$$

where σ is the frequency in $\mu\ m^{-1}$, and f the partial pressure. Applying the above variation in moisture content;

$$(S_L - S_{IR})_f = (S_L - S_{IR}) + f \times 0.0457\ (\sigma_L^2 - \sigma_{IR}^2) \times 10^{-8}$$

where the correction term is $0 < \Delta S < 1.9 \times 10^{-8}$ for $0 < f <$ 18 torr.

Hence $(\sigma_{IRvac})_{H_2O} = (\sigma_{IRvac})\ (1 \begin{smallmatrix} + 1.9 \\ - 0.0 \end{smallmatrix} \times 10^{-8})$.

According to Edlen (1966) the effect of changes in CO_2 concentration normally encountered, cause a change in the refractivity of air which is much less than that due to water vapour changes and hence can be ignored.

In summary provided that a spectral line can be accurately located on the frequency axis, the uncertainty in the absolute value of this frequency will be

$$\sigma_{IRvac} = \sigma_{IRmeas} \begin{cases} 1 \pm 3 \times 10^{-8} & \text{due to laser adjustment} \\ \pm 6 \times 10^{-8} & \text{due to aperture alignment} \\ \pm 22 \times 10^{-8} & \text{due to index of air variations.} \end{cases}$$

2. Experimental Results

2.1 General remarks on the quality of spectra

The results presented here were obtained over a period of about one year from September 1968 to September 1969. By analyzing the results of each run before embarking upon the next spectrum, it was possible to provide useful feedback and hence improve the technique of collecting data and correct for problems quickly as they arose. Also, to make the initial observation of spectral lines simpler, the measurements were started at higher density where relatively strong and broad lines were expected. Only gradually was the density reduced until the lines became too weak to study effectively. As a result of this approach, the spectra obtained for lower densities are generally more reliable, because of the improved experience.

In the experimental set-up there was provision for the observation of six of the Q_1 transitions ($\Delta v = 1$, $\Delta J = 0$) and two S_1 transitions ($\Delta v = 1$, $\Delta J = +2$) namely; Q_1 (0), Q_1 (1), Q_1 (2), Q_1 (3), Q_1 (4), Q_1 (5), S_1 (0) and S_1 (1). Of these transitions, the S_1 (0) line was detected in only a few spectra with long absorption path, and the Q_1 (4) and Q_1 (5) lines were always too weak to be seen. The S lines appear to arise mainly from quadrupole transitions rather than induced-dipole transitions because these lines were present regardless of the presence of the externally applied field. In order to eliminate any spectral details that

are not related to the field induced spectrum of the hydrogen molecules the log-ratio of a spectrum with the field off to a spectrum with the field on is studied, except in the case of the S lines which are not seen in the log-ratio plot.

The taking of the log-ratio of two spectra in order to isolate the lines was somewhat complicated by the fact that each interferogram contained a set of "secondary fringes" resembling the main features of the interferogram but reduced in magnitude by a factor of about 60 and centered at about 13 cm of path difference. These fringes arise from interference due to a beam reflected from the back surface of the separating plate. An analysis of their effect on the spectrum shows that they add a sinusoidal component to all parts of the spectrum having an amplitude proportional to the local intensity (i.e. at zero intensity no sinusoid and at high intensity a large amplitude). This sinusoidal component should disappear when taking the ratio of two spectra; however, the exact location along the path difference axis of these fringes varies due to thermal expansion of the separating plate, which in turn causes phase shifts in the sinusoidal component of the spectrum. It was found that when these secondary fringes are temporarily set to zero during the Fourier transformation the resulting background (spectrum without applied field) contains no sharp features near any of the lines of interest, and consequently it was felt appropriate to shift the background with respect

to the spectrum a small amount in order to bring the sinusoidal component in phase.

In Fig. 12 are shown small sections of a typical spectrum along with the corresponding background. The above mentioned sinusoidal components are not obvious in this figure because of their relatively long wavelength on this scale (λ = 1.5"). These spectra were obtained from a computer plotted graph (Calcomp) derived from data points that are spaced 0.05" apart. The actual data points obtained during the Fourier transformation of the interferogram would occur at 0.2" intervals in Fig. 12 but the additional data points used to improve the display of the spectrum are obtained by interpolation with a suitable scanning function. Note that noise features in the spectrum are of the same width or wider than the limit of resolution because the noise structure is established before Fourier transformation, and is "analyzed" at the same resolution as the spectrum. In Fig. 13 is shown a plot of the log-ratio of each of the spectral sections shown in Fig. 12. Apart from the broadening by the instrumental line profile, these features should be directly proportional to the absorption coefficient of the gas. It can be seen that the $Q_1(1)$ line can be studied with some detail while it is only possible to estimate the line width for the other transitions. Since the limit of resolution is high, small distortions of the profile due to poor signal to noise ratio do not preclude

FIGURE 12

Typical absorption features

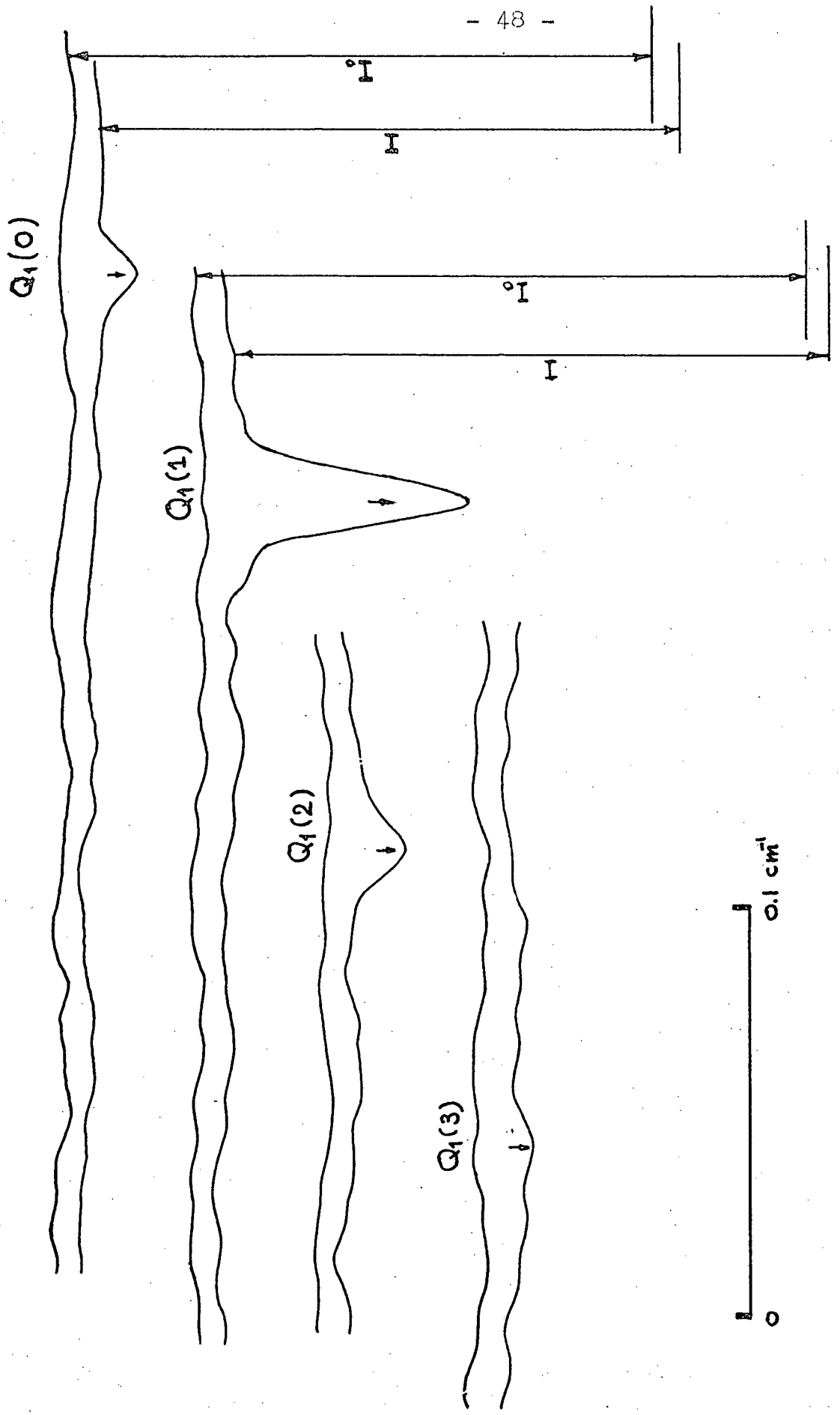
°I
I
°I
I
Q1(0)
Q1(1)
Q1(2)
Q1(3)
0.1 cm⁻¹
0

FIGURE 13

Log ratio plots of absorption features shown in Fig. 12

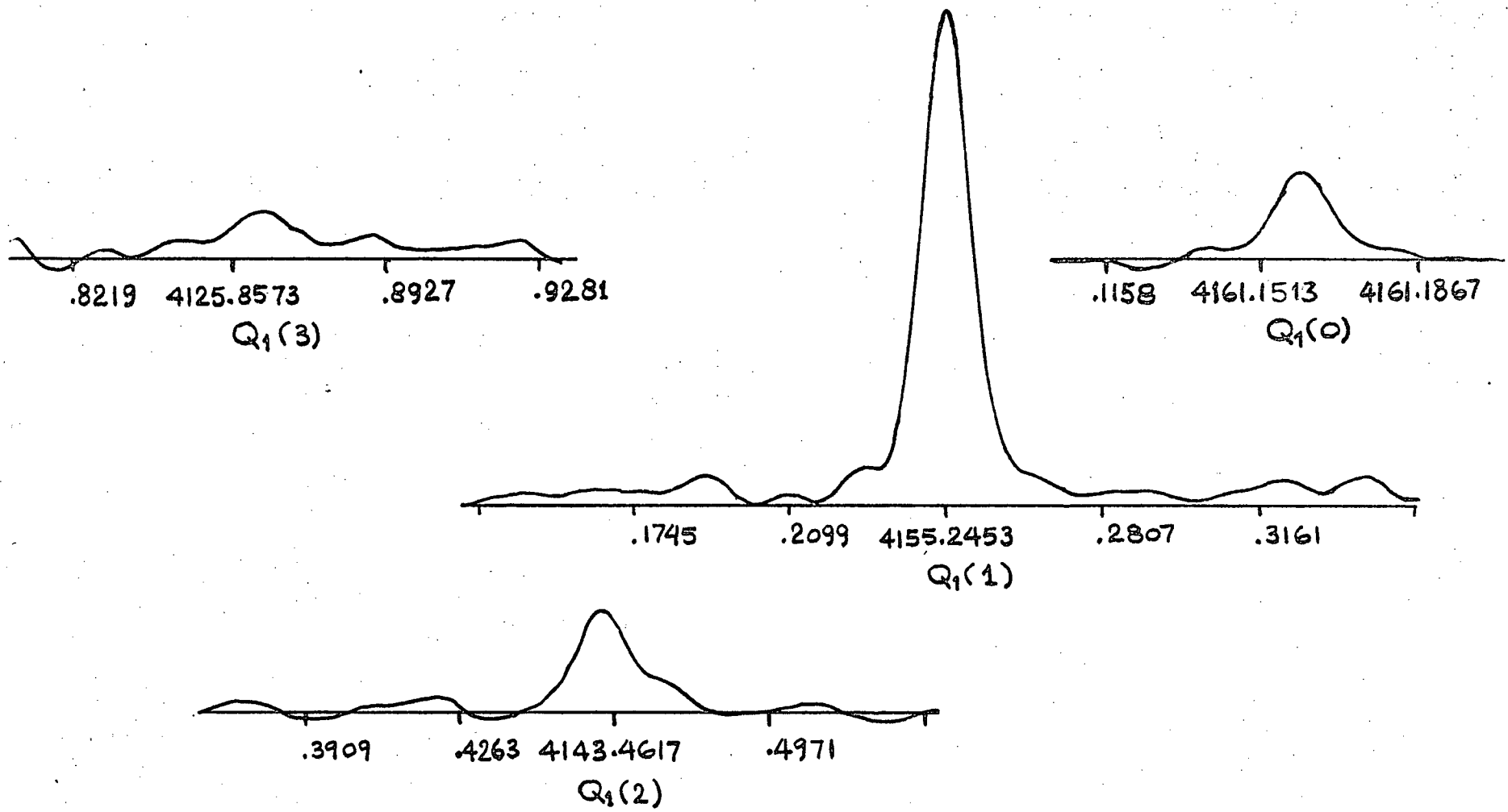
.8219
4125.8573
.8927
.9281
$Q_1(3)$
.1158
4161.1513
4161.1867
$Q_1(0)$
.1745
.2099
4155.2453
.2807
.3161
$Q_1(1)$
.3909
.4263
4143.4617
.4971
$Q_1(2)$

the accurate determination of the central frequency of the weak lines. Hence the list of frequencies is more complete than the determination of other parameters.

In Fig. 14 is shown a sequence of profiles for the $Q_1(1)$ transition taken at different densities to demonstrate the change in line width and central frequency as a function of density. The profiles correspond to different electric field strengths and densities, and for this reason they have quite different areas.

2.2 Frequencies of the transitions

The Fourier analysis was performed on an interferogram obtained by numerically filtering the original interferogram. As a result, the frequencies corresponding to the spectral amplitudes calculated were not very simply related to the index used in the computer program identifying the amplitude. The relation is described here.

Frequencies are determined from the computer data by taking the ratio of the number of spectral points from the zero frequency point, at which the center of the profile occurs, to the total number of points describing the principal alias and then multiplying this ratio by the sample frequency. If the original line did not occur in the principal alias, the starting frequency of the alias in question is assigned to the zero frequency point and thus becomes an additive term. The recipes for the evaluation of

FIGURE 14

Sequence of profile for $Q_1(1)$ transition at different density

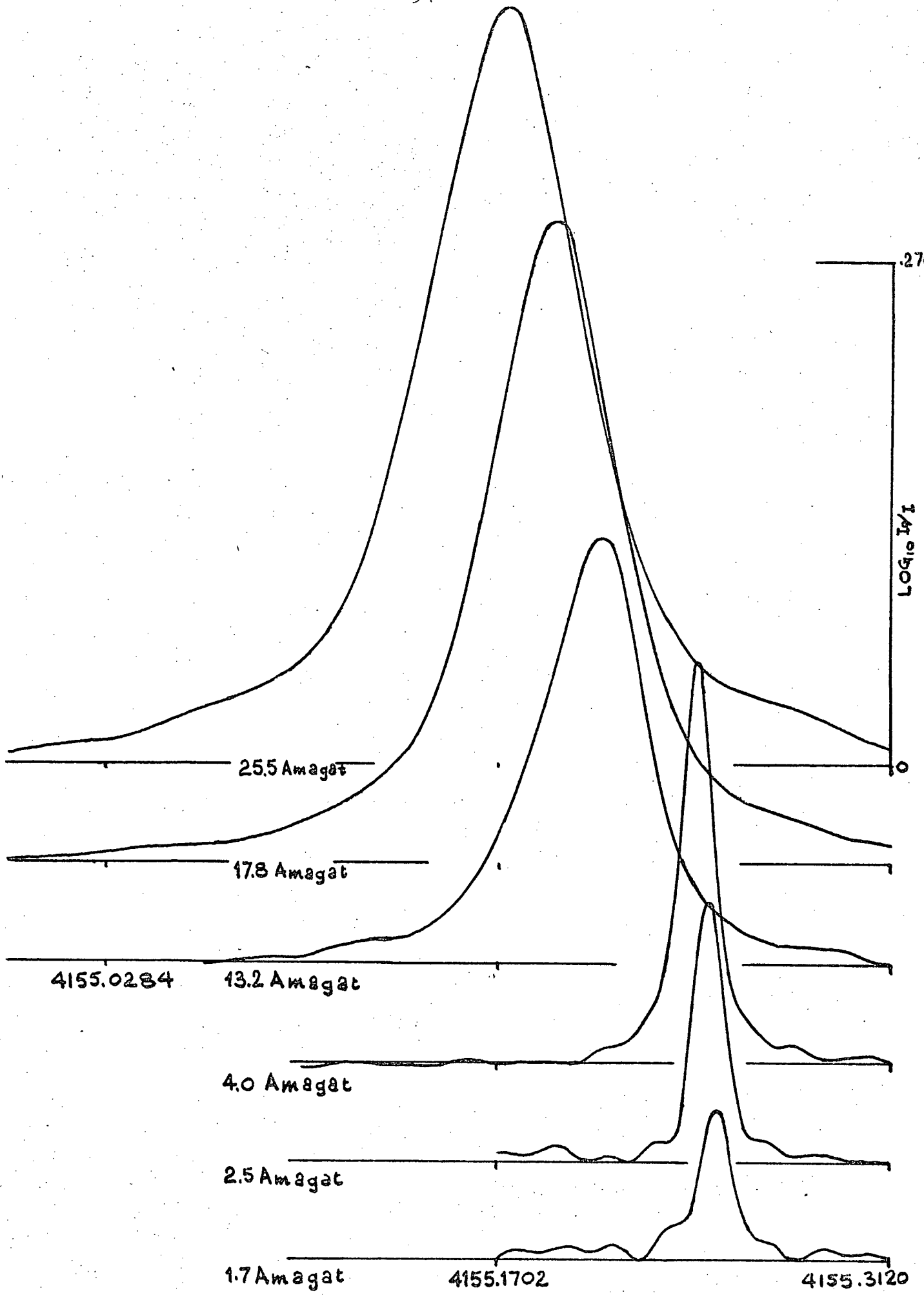
.270
0
LOG_{10} I/I
25.5 Amagat
17.8 Amagat
4155.0284
13.2 Amagat
4.0 Amagat
2.5 Amagat
1.7 Amagat
4155.1702
4155.3120

the frequencies of the various lines are:

$$\sigma_n = \frac{39.0}{17.0h} - \frac{(n-1)}{N} \times \frac{6.0}{17.0h} \quad \text{for } S_1(0) \text{ line}$$

$$\sigma_n = \frac{38.0}{17.0h} + \frac{(n-1)}{N} \times \frac{6.0}{17.0h} \quad \text{for the } S_1(1) \text{ line}$$

and $$\sigma_n = \frac{2.0}{h} + \frac{(n-1)}{N} \times \frac{6.0}{17.0h} \quad \text{for all Q lines.}$$

where h is very nearly equal to eight times the wavelength of the laser light, n is the number of points to the center of the profile (not necessarily an integer) and N is the total number of points in the principal alias. Aperture corrections for the sample interval and the effect of the refractivity of air are incorporated in the value of h in such a way that the frequencies evaluated above are in vacuum wave numbers. Because of these corrections, the value of h for each observed line is different and also different values of h are used when different aperture diameters are used at the different limits of resolution. Table I gives a list of values for h used in the actual evaluation of the frequencies, and is based on the relation

$$h = 8 \lambda_{vacL} \left(1 - \frac{r_m^2}{4f_c^2} - 4 \times 10^{-8} - (S_L - S_{IR})\right) \text{ (see text)}$$

TABLE I

σ_{IR}	r_m = 1.5 mm	r_m = .91 mm	r_m = .75 mm	r_m = 0.50 mm	x 10^{-8}
cm^{-1}	h in μ m	h	h	h	$S_L - S_{IR}$
4125	5.06390169	5.06390888	5.06391023	5.06391180	364.9
4143	5.06390170	889	1024	1182	364.7
4155	5.06390171	890	1025	1183	364.5
4161	5.06390171	890	1025	1183	364.5
4498	5.06390193	912	1048	1216	359.9
4712	5.06390209	928	1064	1221	356.9

$(S_L - S_{IR})$ is taken at p = 762 torr, t = 21.5°C, partial pressure of H_2O = 10 torr

λ_{vacL} = .6329914 μ m.

f_c = 500 mm

Uncertainties in the above values of h as mentioned earlier in the text may cause an uncertainty in the calibration of the frequency axis of 1 part in 3 x 10^6 which corresponds to $\pm$ 1.4 x 10^{-3} cm^{-1} at 4150 cm^{-1}. The accuracy with which the spectral lines can be located depends on the signal to noise ratio in the spectrum and to some extent on the width of the observed line. To determine precisely the center of the profile, the number of points describing the spectrum was increased by a factor of four by means of interpolation with a known scanning function and then the log-ratio of this enlarged set of data was plotted by the "Calcomp plotter". The bisector of this plotted profile is drawn in by hand and its predominant position is then taken as the center of the profile. The frequencies thus obtained were graded with

small letters to indicate over how wide a frequency band the bisector is located.* (a = within 0.001 cm^{-1}, b = within 0.004 cm^{-1}, c = within 0.008 cm^{-1}). In Table II is shown a list of frequencies at the various densities.

At some densities spectra have been repeated in order to check the reliability of the results. In particular at 5.90 amagats density, four spectra were recorded each at a different field strength to determine if there exists a frequency shift as a function of field strength. The data for these spectra was collected over a period of about 20 hours so that atmospheric conditions would be very nearly the same. The frequencies of the four $Q_1(1)$ lines are found to be the same to within $\pm$ 0.0005 cm^{-1}. See Fig. 15 for a plot of this group of $Q_1(1)$ lines. This test seems to indicate that there is no frequency shift as a function of field strength. However, deviations from a regular density dependence of the observed frequencies appear to be slightly correlated with the applied field strength, but the accuracy of these results is insufficient to establish this correlation.

The values of the density were obtained from the pressure of the hydrogen gas in the absorption cell using the pressure-temperature-density tables of the National Bureau of

* this was not done for the S lines and some of the last results.

TABLE II

List of frequencies of the lines studied at various densities.

TABLE II

LINE POSITIONS

DENSITY AMAGAT	APP.FIELD KV/cm	ABS.PATH m	$Q_1(0)$ cm^{-1}	$Q_1(1)$ cm^{-1}	$Q_1(2)$ cm^{-1}	$Q_1(3)$ cm^{-1}	$S_1(0)$ cm^{-1}	$S_1(1)$ cm^{-1}	RESOLUTION LIMIT cm^{-1}
28.4	75.3	1.0 m	4161.1056[b]	4155.1639[b]	4143.4129[b]	4125.8087[c]		4712.8504	0.028
25.4	71.8	1.0	.1138[a]	.1774[a]	.4199[b]	.8304[a]		.8604	"
22.4	57.5	1.0	.1179[a]	.1832[a]	.4272[c]	.828 [b]		-.	"
17.8	71.8	1.0	.1254[b]	.1949[a]	.4309[c]	.840 [c]		-.	"
13.3	64.6	1.0	.1363[c]	.2109[b]	.4335[c]	.848 [c]		-.	"
10.2	68.9	1.0	.1420[b]	.2178[b]	.4403[b]	.8557[b]		.8835	0.014
8.22	50.6	1.0	.1470[b]	.2272[a]	.4465[b]	.8565[b]		-.	"
7.73	57.5	1.0	.1447[b]	.2250[b]	.4452[b]	.852 [b]		-.	"
7.13	50.3	1.0	.1473[b]	.2292[a]	.4494[b]	.853 [c]		-.	"
5.90	46.7	1.0	.1500[a]	.2314[a]	.4511[a]	.862		-.	"
5.90	9.33	4.0	-.	.2345[a]	-.	-.		.8917	0.007
5.90	16.8	4.0	-.	.2347[a]	-.	-.		.8898	"
5.90	22.4	4.0	-.	.2345[a]	.4554[b]	-.		.8922	"
5.90	27.1	4.0	-.	.2338[a]	-.	-.		.897	"
5.26	18.7	4.0	.1548[b]	.2368[a]	.4557[b]	.861 [c]		.8927	"
5.26	24.6	4.0	.1539[b]	.2368[a]	.4547[b]	.863 [c]		.894	"
4.62	35.8	1.0	.1541[b]	.2369[a]	.4547[b]	.865 [c]		-.	0.014
4.62	21.0	4.0	.1531[b]	.2381[a]	-.	-.		.8987	0.007
4.62	25.6	4.0	.1568[a]	.2381[a]	.4548[b]	.861 [c]		.8988	0.007
4.00	27.6	4.0	.1560[b]	.2410[a]	.4537[b]	.864 [b]		.8985	0.014
4.00	25.2	4.0	.1563[a]	.2409[a]	.4570[a]	.8658[b]		.8951	0.007
3.40	25.2	4.0	.1578[b]	.2426[a]	.4600[b]	.8648[b]		.8962	"
2.90	25.2	4.0	.1601[b]	.2438[b]	-.	-.		.8967	"
2.45	25.1	4.0	.1601[a]	.2452[a]	.4600[b]	.8654[b]		.8962	"
2.08	25.6	4.0	.1593[b]	.2481[a]	.4614[a]	.8690[b]		.8997	"
1.70	25.6	4.0	.1610[b]	.2480[a]	.4625[b]	.8697[b]		.8995	"
2.53	16.8	4.0	.159	.246	.461	.864		.897	0.0055
2.53	0.0	44.0	-.	.247	-.	-.	-.	.898	"
1.94	16.4	44.0	.1592	.246	.461	.864	4497.835	.895	"
1.50	16.4	44.0	.1600	.247	.463	-.	.840	.899	"
1.50	16.4	44.0	.1630	.247	.459	-.	.838	.897	"
1.10	16.4	44.0	-.	-.	-.	-.	.854	.897	"
.78	16.4	44.0	-.	.246	.455	-.	.840	.892	"

FIGURE 15

Sequence of 4 profiles for $Q_1(1)$ transition at same density and different field strength

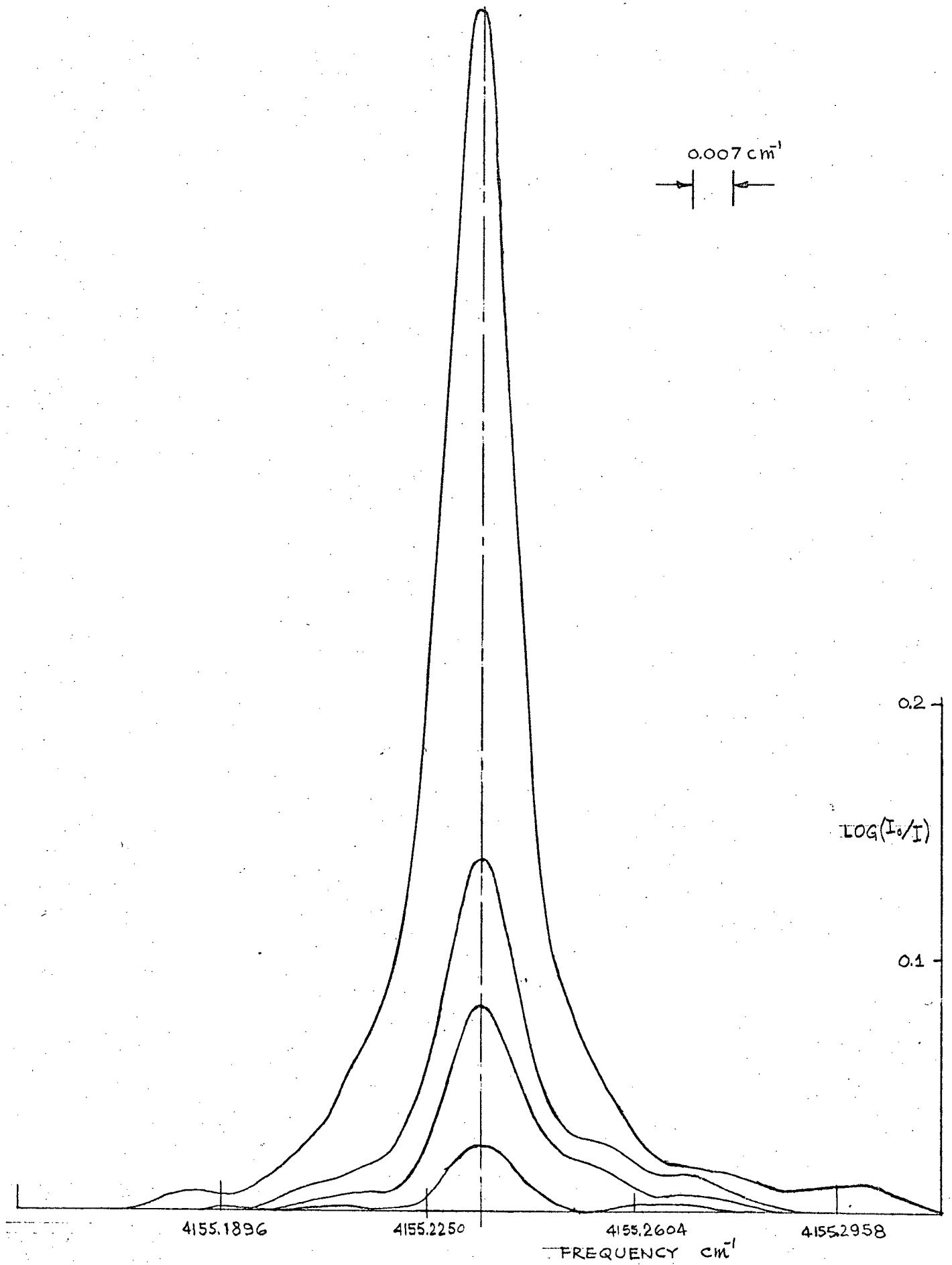
0.007 cm⁻¹
0.2
LOG(I₀/I)
0.1
4155.1896
4155.2250
4155.2604
4155.2958
FREQUENCY cm⁻¹

Standards. The pressures for the five highest density spectra were measured with a 0 - 1000 psi Bourdon gauge giving about ± 5% accuracy. Below 11 amagats density, pressures were measured with a 0 - 300 psi Bourdon gauge with an accuracy of ± 1% of full scale. In later experiments at densities below 2.4 amagats, pressures were measured simultaneously with a Mercury Manometer and the 0 - 300 psi Bourdon gauge giving pressures accurate to about ± 1% of the measured value.

In Figs. 16, 17, 18, 19 and 20 are shown plots of frequency vs. density for the different lines studied. In these figures are also shown some of the results obtained by other investigations of the hydrogen spectrum.

2.3 Line profiles

In general, the limit of resolution with which the spectra were recorded was not low enough to reveal accurately the functional form of the line profiles. However, an attempt has been made to correct for the effect of the instrumental line profile on the actual form of the absorption feature.

In Fourier transform spectroscopy the instrumental line shape function is essentially independent of the geometrical arrangement of the instrument (i.e. it is not related to the quality of the optics such as the flatness of the beam splitter, etc.). Instead it depends on the steadiness of the "fringe visibility", and on the maximum path length achieved. The alignment of the interferometer during

FIGURE 16

Graph showing frequency shift and line width vs. density for $Q_1(0)$ line

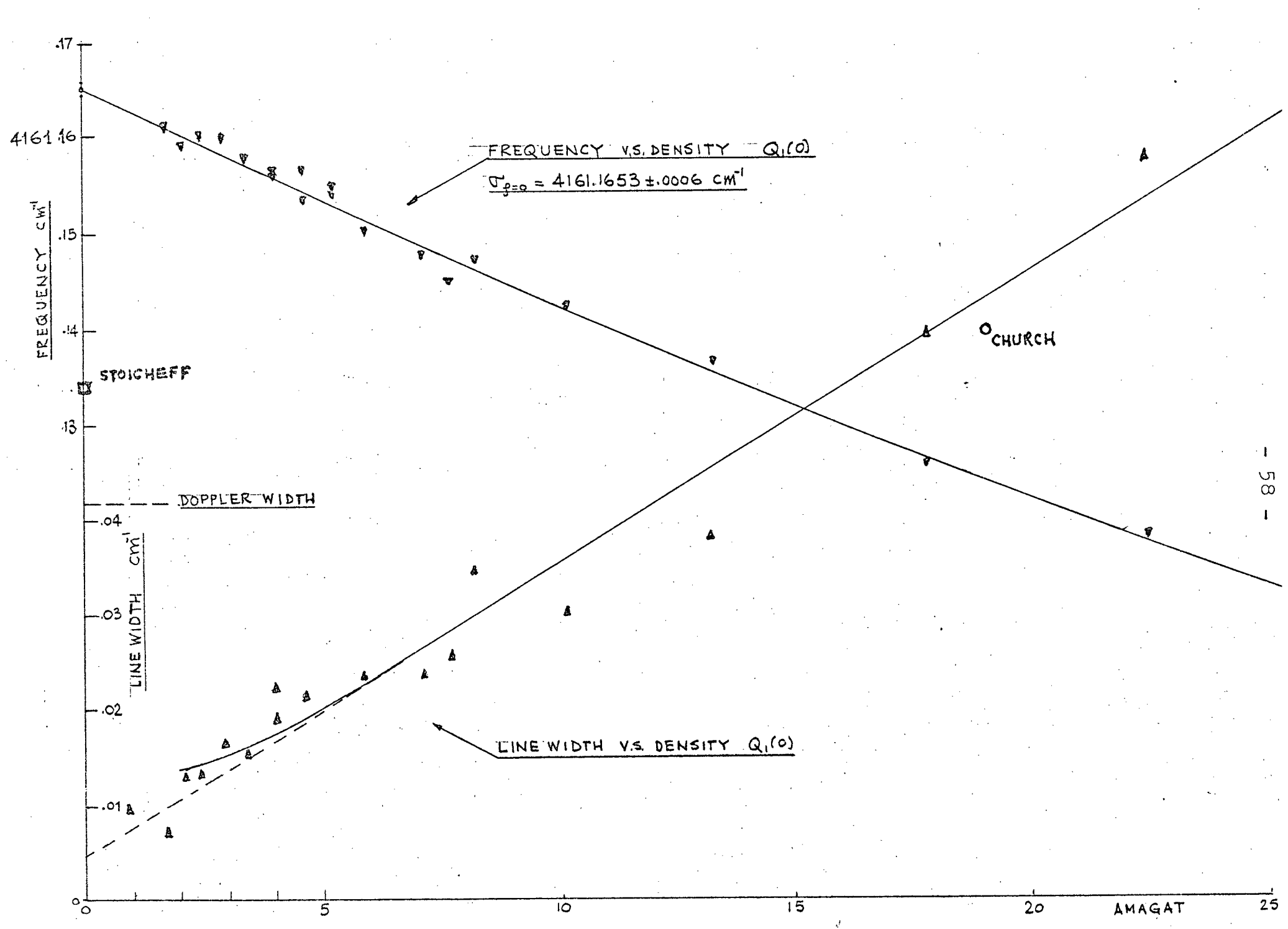
FREQUENCY V.S. DENSITY Q1(0)
$\sigma_{\rho=0}$ = 4161.1653 ± .0006 cm⁻¹
LINE WIDTH V.S. DENSITY Q1(0)
DOPPLER WIDTH
STOICHEFF
CHURCH
FREQUENCY cm⁻¹
LINE WIDTH cm⁻¹
AMAGAT
4161.16
.17
.15
.14
.13
.04
.03
.02
.01
0
5
10
15
20
25

FIGURE 17

Graph showing frequency shift and line width vs. density for $Q_1(1)$ line

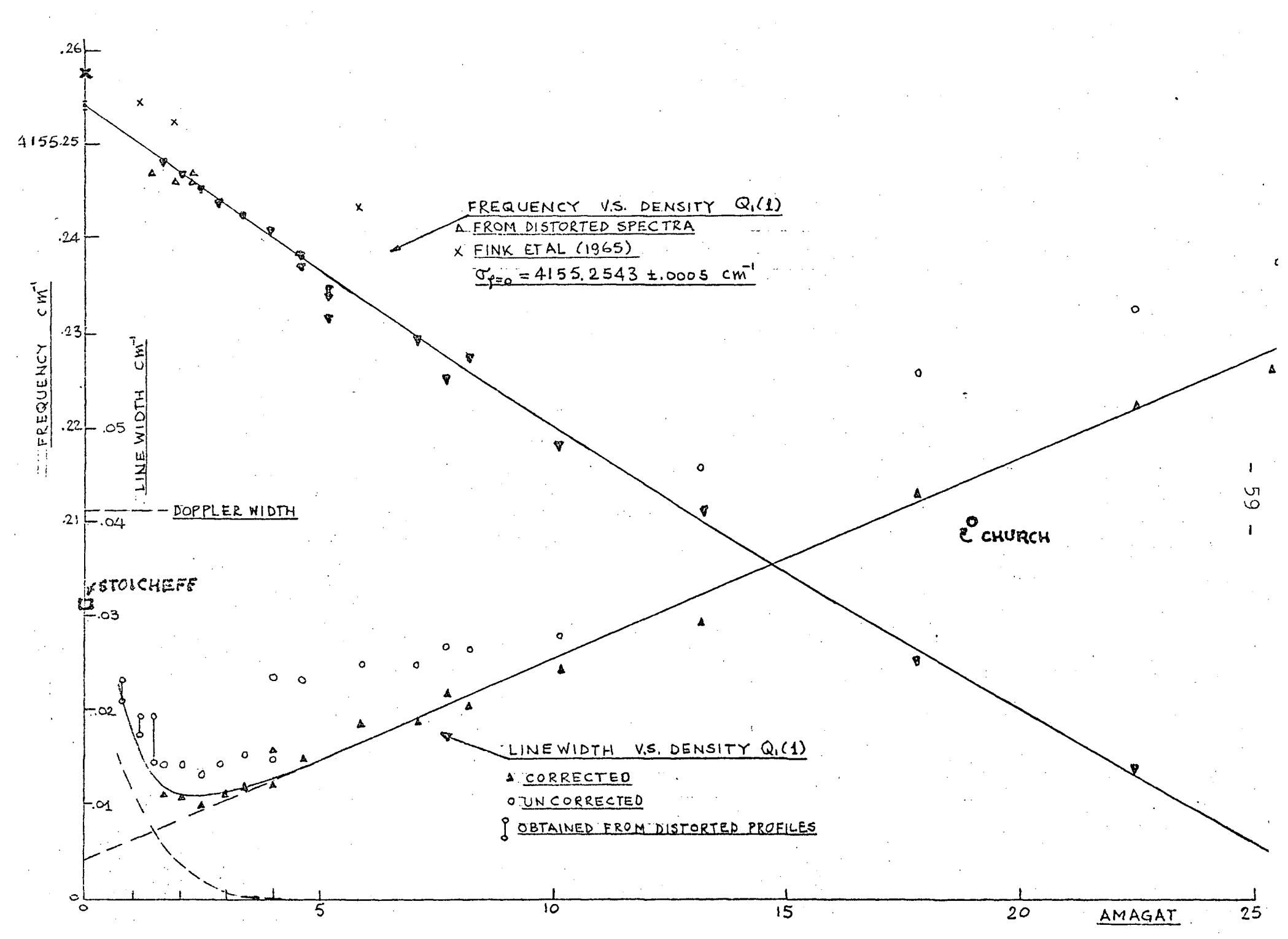
FREQUENCY V.S. DENSITY $Q_1(1)$
Δ FROM DISTORTED SPECTRA
× FINK ET AL (1965)
$\sigma_{f=0} = 4155.2543 \pm .0005\ cm^{-1}$
LINEWIDTH V.S. DENSITY $Q_1(1)$
▲ CORRECTED
○ UNCORRECTED
OBTAINED FROM DISTORTED PROFILES
DOPPLER WIDTH
STOICHEFF
CHURCH
FREQUENCY cm^{-1}
LINE WIDTH cm^{-1}
AMAGAT
4155.25
.26
.24
.23
.22
.21
.05
.04
.03
.02
.01
0
5
10
15
20
25
1-59-1

FIGURE 18

Graph showing frequency shifts and line width vs. density for $Q_1(2)$ line

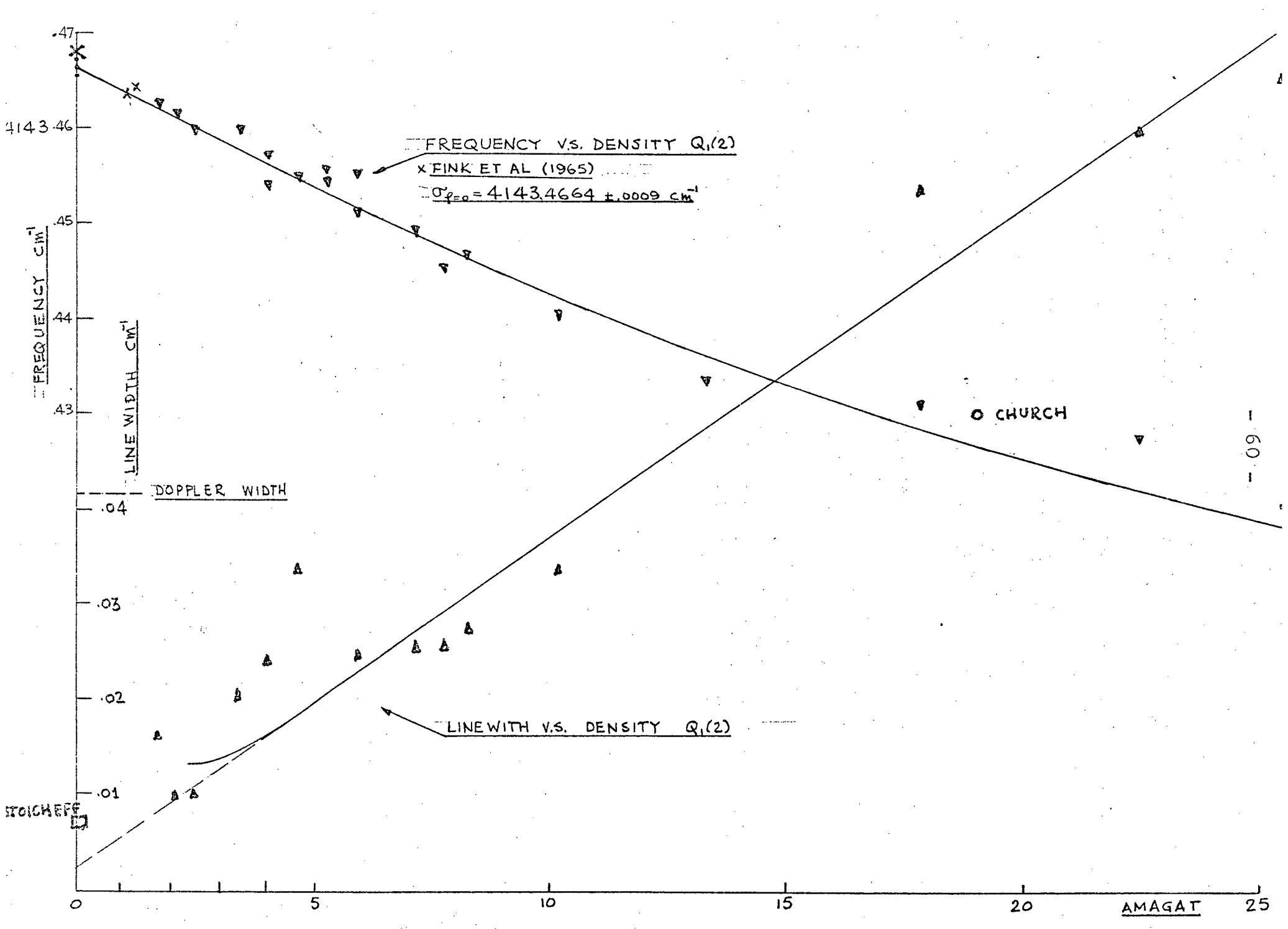
FREQUENCY V.S. DENSITY $Q_1(2)$
x FINK ET AL (1965)
$\sigma_{\rho=0} = 4143.4664 \pm .0009\ cm^{-1}$
O CHURCH
LINEWITH V.S. DENSITY $Q_1(2)$
DOPPLER WIDTH
FREQUENCY cm^{-1}
LINE WIDTH cm^{-1}
AMAGAT
STOICHEFF
.47
4143.46
.45
.44
.43
.04
.03
.02
.01
0
5
10
15
20
25

FIGURE 19

Graph showing frequency shift and line width vs. density for $Q_1(3)$ line

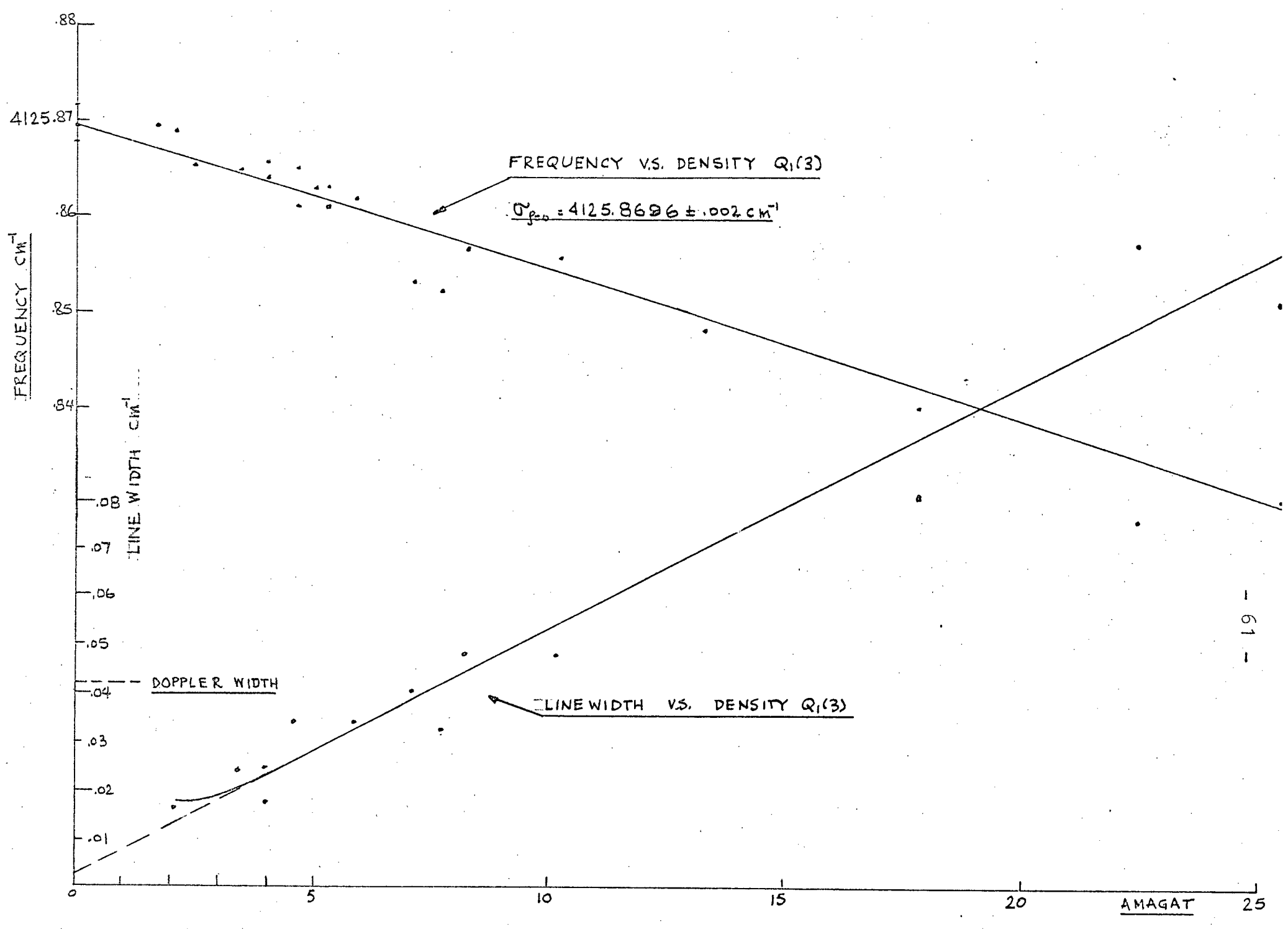
.88
4125.87
.86
.85
.84
FREQUENCY CM⁻¹
LINE WIDTH CM⁻¹
.08
.07
.06
.05
.04
.03
.02
.01
DOPPLER WIDTH
FREQUENCY V.S. DENSITY Q₁(3)
σ₀₌₀ = 4125.8696 ± .002 CM⁻¹
LINE WIDTH V.S. DENSITY Q₁(3)
0
5
10
15
20
25
AMAGAT
1-61

FIGURE 20

Graph showing frequency shift vs. density for the $S_1(0)$ and $S_1(1)$ lines

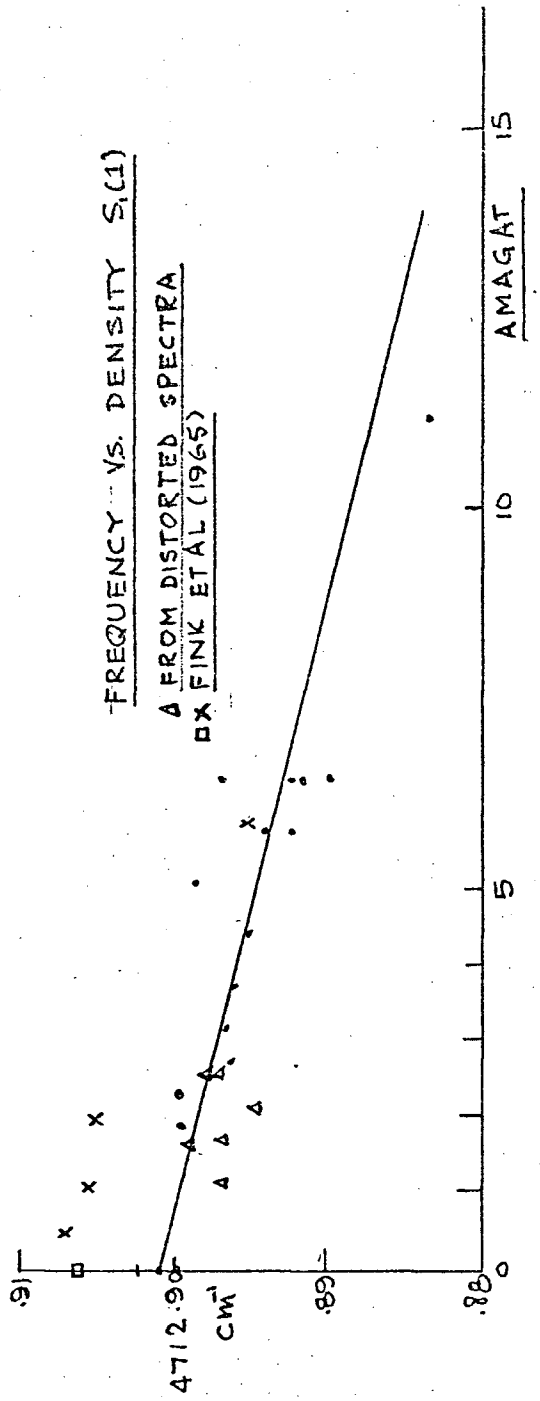
FREQUENCY VS. DENSITY S,(1)
Δ FROM DISTORTED SPECTRA
□× FINK ETAL (1965)
.91
.89
.88
4712.90
cm⁻¹
0
5
10
15
AMAGAT

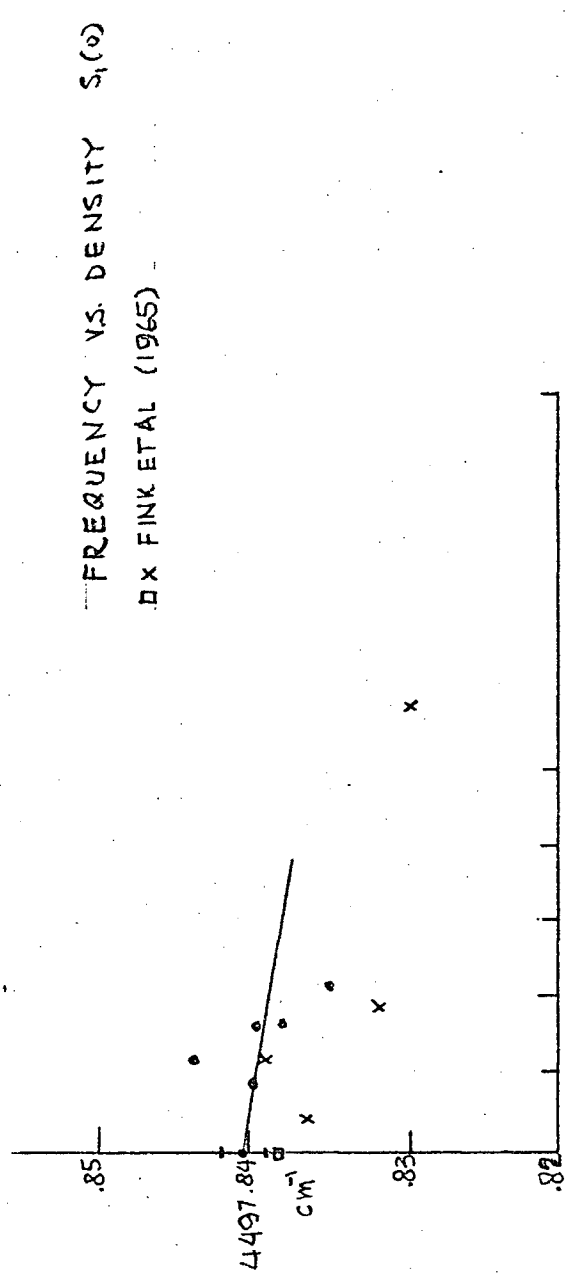
FREQUENCY VS. DENSITY S,(0)
□× FINK ETAL (1965)
.85
.83
.82
4497.84
cm⁻¹
0
5
10
AMAGAT

each experiment is continuously monitored by means of the amplitude of the reference fringes; this amplitude remained steady. Since the detector records the total intensity passing through the entrance aperture of the interferometer a reduction in fringe visibility occurs towards long path difference where the fringes become so small that the interference condition is no longer uniform over the surface of the aperture. Then the effect of the instrument upon the actual spectral profile, which is representable by an infinitely long interferogram is to broaden this profile because of attenuation and truncation of its Fourier transform (interferogram). The procedure used to determine the most probable form of the Q line profile was as follows:

1) We assume a possible form for the profile and specify its width and height to be equal to the observed width and height.

(i.e. $\ln\left[I_0(\sigma)/I(\sigma)\right] = A_{OBS.}\, e^{-\sigma^2/(\Delta\sigma^2_{OBS.}\ln 2)}$ for Gaussian estimate

or $\ln\left[I_0(\sigma)/I(\sigma)\right] = \dfrac{A_{OBS.}\ \Delta\sigma^2_{OBS.}}{\Delta\sigma^2_{OBS.} + \sigma^2}$ for Lorentzian estimate.

2) The exponential of the above function, which looks like an absorption feature in a unity height background, is broadened by the instrumental line shape function. This is accomplished by simply attenuating and truncating the Fourier transform of this absorption feature in a manner similar to that which takes place in the interferometer.

3) The log ratio of this broadened feature is compared with the observed profile. At first a simple comparison of peak height and halfwidth is used to adjust the parameters of the analytic function of the profile until by means of successive iterations the peak height and width of the broadened analytical function matches the observed values to within about 1%.

If the choice of initial function is correct, graphs of the synthetic spectrum and observed spectrum should coincide. The success of this procedure is indicated in Fig. 21 where the solid curves indicate the synthetic profiles and the dashed sections show the departure of the observed spectrum from the synthetic spectrum. As can be seen, the Lorentz profile seems to be the most satisfactory fit for the densities shown. If it is assumed that the underlying profiles are Lorentz profiles in form, then a list of parameters for the profiles that fit the data best can be compiled. The width at half height values thus obtained are quite reliable for the strong $Q_1(1)$ line, but are not too reliable for the weaker lines because of poorer signal to noise ratio. In Table III is shown a list of linewidths for the different transitions and densities including the observed uncorrected width and the width of the best synthetic profile. Also shown in Table III is the integrated intensity of the synthetic profile divided by the length of the absorption path, the square of the field strength and the density.

FIGURE 21

Comparison of observed profile with broadened Lorentz profile and broadened Gaussian profile

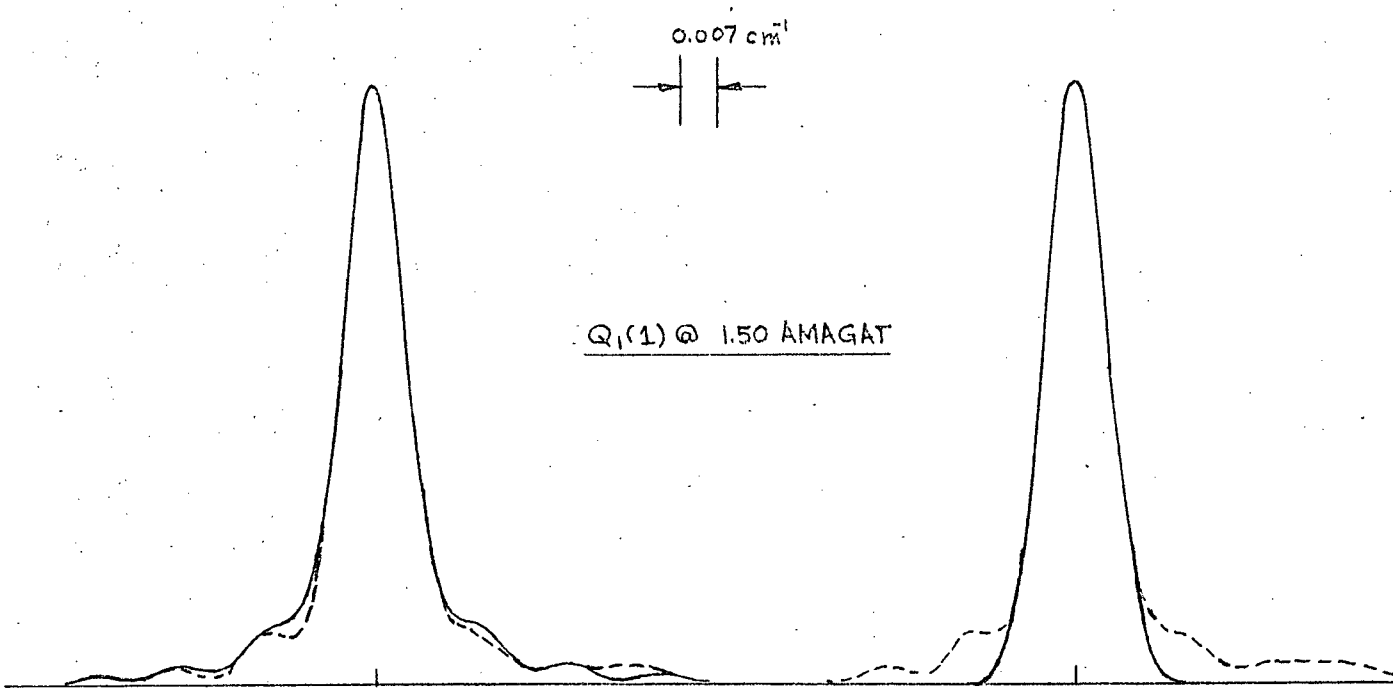

FIT OF LORENTZ PROFILE

FIT OF GAUSSIAN PROFILE

DASHED LINE CORRESPONDS TO OBSERVED PROFILE

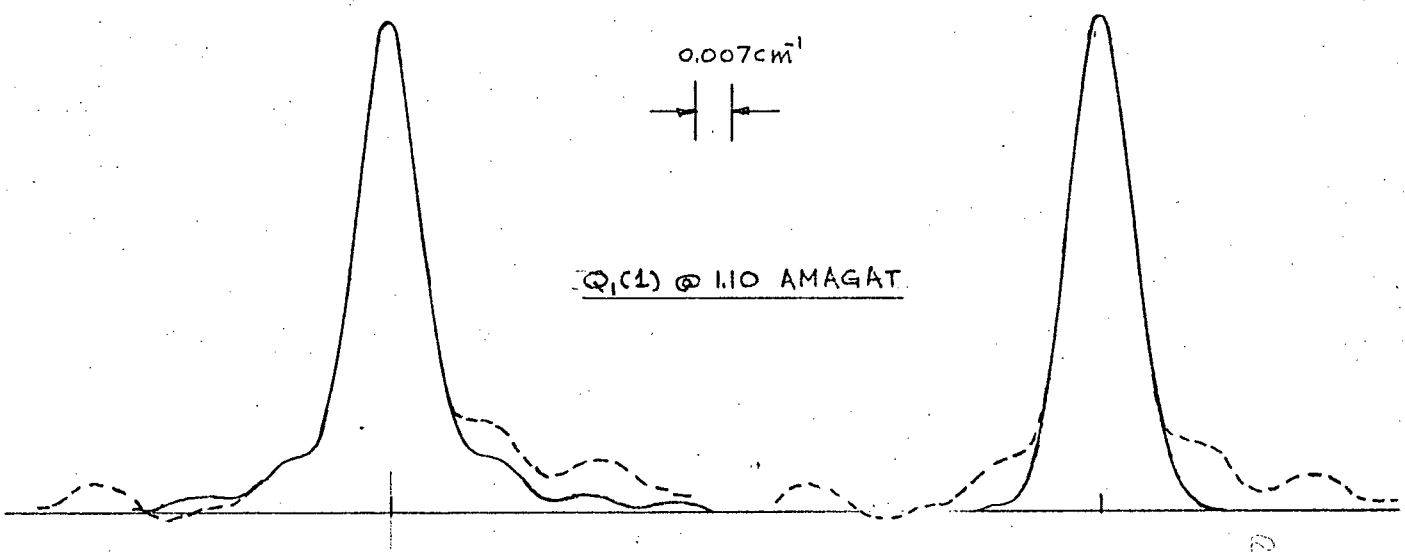

TABLE III

List of observed linewidth and calculated width and height of Lorentz profiles that fit the observed data. Also a list of normalized integrated absorption coefficients; all related to density.

TABLE III

DENSITY AMAGAT	$Q_1(0)$ OBS. WIDTH cm^{-1}	$Q_1(0)$ CALCULATED WIDTH cm^{-1}	$Q_1(0)$ CALCULATED HEIGHT $\log(I_o/I)_m$	$Q_1(0)$ INT.ABS. $B/\rho 1E^2$	$Q_1(1)$ OBS. WIDTH cm^{-1}	$Q_1(1)$ CALCULATED WIDTH cm^{-1}	$Q_1(1)$ CALCULATED HEIGHT $\log(I_o/I)_m$	$Q_1(1)$ INT.ABS. $B/\rho 1E^2$	$Q_1(2)$ OBS. WIDTH cm^{-1}	$Q_1(2)$ CALCULATED WIDTH cm^{-1}	$Q_1(2)$ CALCULATED HEIGHT $\log(I_o/I)_m$	$Q_1(2)$ INT.ABS. $B/\rho 1E^2$	$Q_1(3)$ OBS. WIDTH cm^{-1}	$Q_1(3)$ CALCULATED WIDTH cm^{-1}	$Q_1(3)$ CALCULATED HEIGHT $\log(I_o/I)_m$	$Q_1(3)$ INT.ABS. $B/\rho 1E^2$
28.4	.085	.0774	.124	2.14	.0638	.0548	.823	10.1	.087	.079	.097	1.71	.141	.135	.052	1.56
25.4	.085	.0768	.102	2.16	.0673	.0555	.720	11.0	.092	.085	.091	2.14	.128	.121	.047	1.57
22.4	.084	.0777	.070	2.65	.0623	.0521	.471	12.0	.085	.079	.064	2.50	.135	.135	.036	2.41
17.8	.069	.0592	.102	2.37	.0553	.0428	.643	10.8	.082	.074	.084	2.43	.089	.081	.054	1.71
13.3	.052	.0380	.075	1.86	.0454	.0291	.497	9.4	.052	.038	.057	1.39	.078	.070	.043	1.95
10.2	.033	.0302	.090	2.02	.0277	.0239	.704	12.6	.036	.034	.085	2.12	.049	.048	.045	1.59
8.22	.041	.0398	.046	3.16	.0262	.0203	.342	11.9	.031	.027	.044	2.05	.049	.049	.026	2.17
7.73	.030	.0258	.042	1.52	.0266	.0216	.388	11.8	.030	.026	.050	1.85	.035	.033	.033	1.50
7.13	.028	.0234	.049	2.29	.0248	.0187	.301	11.3	.030	.025	.036	1.82	.043	.041	.024	1.98
5.9	.028	.0234	.041	2.71	.0248	.0185	.228	11.8	.029	.024	.037	2.55	.037	.034	.017	1.63
4.62	.027	.0217	.027	3.53	.0230	.0148	.152	13.7	.035	.034	.022	4.50	.035	.034	.016	3.26
4.00	.028	.0226	.048	3.24	.0234	.0160	.285	13.6	.029	.024	.040	2.87	.029	.024	.029	2.10
4.00	.020	.0182	.058	3.73	.0148	.0118	.373	15.6	.018	.016	.041	2.34	.019	.017	.030	1.99
3.40	.018	.0156	.054	3.52	.0152	.0117	.344	16.8	.021	.020	.037	3.20	.024	.024	.027	2.62
2.90	.019	.0168	.041	3.38	.0142	.0109	.301	16.1	-	-	-	-	-	-	-	-
2.45	.016	.0134	.041	3.24	.0131	.0092	.260	14.0	.014	.0102	.034	2.03	-	-	-	-
2.08	.0158	.0132	.041	3.59	.0142	.0109	.207	14.9	.014	.0098	.036	2.31	.018	.016	.022	2.31
1.70	.012	.0071	.020	1.16	.0142	.0108	.147	12.8	.018	.0163	.018	2.38	-	-	-	-

The length of the absorption path can be measured to an accuracy of about $\pm$ .5% for each absorption cell used. The accuracy with which the density is known has been discussed earlier. The greatest source of error in the absolute intensity of the lines lies, however, in our knowledge of the applied electric field. The voltage applied to the electrodes was read from the dial of our regulated high voltage supply. The dial readings were calibrated against a J. Fluke high voltage supply at the lower end of the scale. Then the linearity was checked with a voltage divider network and an H.P. vacuum tube voltmeter. Thus the applied voltage is believed to be accurate to within $\pm$ 3%. However, it should be noted that a 100 M resistor was used in series with the supply to prevent damage due to large currents when a discharge occurs in the cell. The gap between the electrodes of the 1 m long cell was 3.12 $\pm$ .09 mm and was not very uniform. The gap between the electrodes of the 4 m cell was measured to be 12 $\pm$ .5 mm and was fairly uniform, but because of the presence of a glass cylinder and rubber potting compound between the electrodes the field in the gas space may have been somewhat distorted (see Fig. 2b for cross section of cell). Because of these factors it is believed that the field strength quoted is accurate to about $\pm$ 10% only.

A test of the accuracy of the line width obtained by the above analysis is the continuity of a plot of line

width vs. density. The uncorrected line widths fall on a highly discontinuous curve because of the abrupt changes in the limit of resolution at which spectra were recorded. In Fig. 17 both the uncorrected and corrected line width as a function of density are shown for comparison. In Figs. 16, 18 and 19 are shown graphs of line width vs. density for the other transitions.

3. Discussion of Results

3.1 Remarks

From the results compiled in Chapter 2 it is possible to deduce various quantities. These are:

1) frequencies as a function of gas density and in particular extrapolated values for zero density,

2) the width and shape of the line profiles as a function of density,

3) the integrated intensities of the lines.

In what follows we attempt to extract as much information as possible about the free molecule of hydrogen and its interactions with its neighbours in the gas. Our conclusions will be compared, wherever possible, with those reached by other writers.

3.2 Zero density frequencies and the molecular constants

The energy level terms for the hydrogen molecule in the $^1\Sigma_g^+$ electronic state (ground state) are given by the equation

$$T(v,J) = G(v) + F_v(J)$$

(Herzberg, 1950)

$$G(v) = w_e\left(v + \tfrac{1}{2}\right) - w_e x_e \left(v + \tfrac{1}{2}\right)^2 + w_e y_e \left(v + \tfrac{1}{2}\right)^3 + \ldots$$

$$F_v(J) = B_v J(J+1) - D_v J^2 (J+1)^2 + H_v J^3 (J+1)^3 + \ldots$$

and

$$B_v = B_e - \alpha_e \left(v + \tfrac{1}{2}\right) + \gamma_e \left(v + \tfrac{1}{2}\right)^2 + \ldots$$

$$D_v = D_e + \beta_e (v + \tfrac{1}{2}) + \delta_e (v + \tfrac{1}{2})^2,$$

and $H_v \cong H_e \cong H_1$.

The transitions observed in these experiments are v' = 0 to v'' = 1 with $J'' = J'$ for J' = 0, 1, 2, 3 and $J'' = J' + 2$ for J' = 0, 1. The $\Delta J = 0$ transitions are denoted by $Q_v(J)$ where v is the quantum number of the final vibrational state and J takes values occurring in the initial state, and then $\Delta J = 2$ transitions are indicated by $S_v(J)$. It may be shown that:

$$\sigma_{Q_1(0)} = \sigma_{1-0} = w_e - 2w_e x_e + {}^{13}/_4\, w_e y_e \qquad (1)$$

$$\sigma_{Q_1(1)} = \sigma_{1-0} + (B_1 - B_0)2 - (D_1 - D_0)4 + (H_1 - H_0)8 \qquad (2)$$

$$\sigma_{Q_1(2)} = \sigma_{1-0} + (B_1 - B_0)6 - (D_1 - D_0)36 + (H_1 - H_0)216 \qquad (3)$$

$$\sigma_{Q_1(3)} = \sigma_{1-0} + (B_1 - B_0)12 - (D_1 - D_0)144 + (H_1 - H_0)1728 \qquad (4)$$

$$\sigma_{S_1(0)} = \sigma_{1-0} + 6B_1 - 36D_1 + 216H_1 \qquad (5)$$

$$\sigma_{S_1(1)} = \sigma_{1-0} + 12B_1 - 144D_1 + 1728H_1 - 2B_0 + 4D_0 - 8H_0 \qquad (6)$$

In solving for the various constants in the above equations we make use of the relations

$$\sigma_{S_1(0)} - \sigma_{Q_1(2)} = \sigma_{S_0(0)} = 6B_0 - 36D_0 + 216H_0 \qquad (7)$$

$$\sigma_{S_1(1)} - \sigma_{Q_1(3)} = \sigma_{S_0(1)} = 10B_0 - 140D_0 + 1720H_0 \qquad (8)$$

$$\sigma_{S_1(2)} - \sigma_{Q_1(4)} = \sigma_{S_0(2)} = 14B_0 - 364D_0 + 7784H_0. \qquad (9)$$

From these three equations we can obtain values for the constants B_0, D_0 and H_0 which can then be used in equations (2), (3), (4) and (6) to solve for B_1, D_1 and H_1. In Table IV is given a list of frequencies extrapolated to zero density by a least squares fitting of a quadratic expansion for frequency v.s. density:

TABLE IV

Line	Frequency
$Q_1(0)$	4161.1653 ± .0006 cm^{-1}
$Q_1(1)$	4155.2543 ± .0005
$Q_1(2)$	4143.4664 ± .0009
$Q_1(3)$	4125.8696 ± .002
$S_1(0)$	4497.8405 ± .002
$S_1(1)$	4712.9008 ± .0014

Note: the tolerance is the computed r.m.s. deviation for the data used in the least squares program.

From the above list of frequencies it is clear that there are no data available for equation (9), and a solution cannot be obtained for B_0, D_0 and H_0. However, the differences computed in (7) and (8) may be compared with frequencies of the pure rotation lines obtained by Stoicheff (1957). We find a small apparent systematic shift in Stoicheff's results in agreement with Fink et al (1965). Using the corrected frequency of Stoicheff for $\sigma_{S_0(2)}$ we can then obtain values for B_0, D_0 and H_0. They are:

Present results	Stoicheff
$B_0 = 59.3344 \pm 6 \times 10^{-4}$ cm^{-1}	$B_0 = 59.3392$ cm^{-1}
$D_0 = +0.04560 \pm 8 \times 10^{-5}$ cm^{-1}	$D_0 = +0.04599$ cm^{-1}
$H_0 = 4.1 \times 10^{-5} \pm 4.8 \times 10^{-6}$ cm^{-1}	$H_0 = 5.2 \times 10^{-5}$ cm^{-1}

It should be noted that the difference frequencies in equations (7) and (8) involve in each case a line whose frequency has been measured relatively poorly. This is reflected in the accuracy of the values obtained for B_0, D_0 and H_0.

Introducing the new values of B_0, H_0 and D_0 into equations (2), (3) and (4) we obtain:

$$B_1 = 56.37600 \pm 2 \times 10^{-4} \text{ cm}^{-1}$$

$$D_1 = +0.04416 \pm 1 \times 10^{-4} \text{ cm}^{-1}$$

$$H_1 = 3.95 \times 10^{-5} \pm 4 \times 10^{-6} \text{ cm}^{-1}$$

and $$\tilde{\nu}_{1-0} = 4161.1653 \pm 6 \times 10^{-4} \text{ cm}^{-1}$$

Now using frequencies for the overtones, $\tilde{\nu}_{2-0}$, $\tilde{\nu}_{3-0}$, as quoted by Foltz et al, we may obtain new values for w_e, $w_e x_e$ and $w_e y_e$ from the equations:

$$\tilde{\nu}_{1-0} = 4161.1653 = w_e - 2w_e x_e + 13/4\ w_e y_e$$

$$\tilde{\nu}_{2-0} = 8087.006 = 2w_e - 6w_e x_e + 31/2\ w_e y_e$$

$$\tilde{\nu}_{3-0} = 11782.351 = 3w_e - 12w_e x_e + 171/4\ w_e y_e.$$

We find:

$$w_e = 4401.1177 \pm .03 \text{ cm}^{-1}$$

$$w_e x_e = 121.284 \pm .02 \text{ cm}^{-1}$$

$$w_e = 4401.1177 \pm .03 \text{ cm}^{-1}$$
$$w_e x_e = 121.284 \pm .02 \text{ cm}^{-1}$$
$$w_e y_e = .8048 \pm .003 \text{ cm}^{-1}.$$

In Table V frequencies calculated from the above constants are shown and compared with the present and previously published results.

TABLE V

Line	Frequencies cm^{-1}				
	calculated	present	Fink et al	Church[a]	Stoicheff[b]
$Q_1(0)$	4161.1653	.1653	*.181	.170	.138
$Q_1(1)$	4155.2541	.2543	†.2586	.246	.208
$Q_1(2)$	4143.4665	.4664	†.4664	.468	.392
$Q_1(3)$	4125.8693	.8696	†.8710	.871	.835
$S_1(0)$	4497.8389	.8405	.8385	.835	
$S_1(1)$	4712.8989	.9008	†.9066	.846	
$S_1(2)$	4916.9635		17.0118	.873	
$S_1(3)$	5108.2505		.4066	.286	
$Q_2(0)$	8087.006			86.94	

* this value is taken from the field induced spectrum of Foltz et al.

† these values are based on the results of Fink et al, but constitute a slightly improved extrapolation to zero density carried out by Foltz et al.

a) these frequencies have been extrapolated to zero density using known frequency shift coefficients and assuming measurements were made at 19 amagat density.

b) these frequencies have been extrapolated to zero density from 2 amagat density.

The results of Fink et al (1966) were obtained from measurements of the quadrupole spectrum at densities near 1 amagat. Even though Foltz et al (1965) quote another set of frequencies at zero density, these frequencies were obtained from an improved extrapolation to zero density of the data reported by Fink et al. This improvement seems somewhat questionable when one notes that the frequency of the $Q_1(0)$ line is entirely due to the measurements of Foltz and seems in poor agreement with our results. Considering that Church quotes an accuracy of $\pm$ 0.02 cm^{-1} his data agree very well with the present results. More recent results quoted by Brannon, Church and Peters (1968) seem to add little to the older results of Church because the accuracy quoted is about the same. The frequencies measured by Stoicheff in the Raman effect appear to be shifted systematically by - 0.045 cm^{-1}. In connection with this comparison it should be remembered that our frequencies are believed to be correct absolutely to within only $\pm$ 0.0015 cm^{-1}, although the reproducibility from spectrum to spectrum is better, being approximately $\pm$ 0.0008 cm^{-1}, as is clear from Table IV.

Finally we present a list of Dunham's Y parameters for the hydrogen molecule in Table VI (see Dunham, 1932):

TABLE VI

w_e	Y_{10}	$= 4401.118\ cm^{-1}$	D_e	Y_{02}	$= +4.632 \times 10^{-2}\ cm^{-1}$
$w_e x_e$	$-Y_{20}$	$= 121.284$ "	β_e	Y_{12}	$= 0.144 \times 10^{-2}$
$w_e y_e$	Y_{30}	$= .8048$"	π_e	Y_{22}	$= 0.0 \pm .0001$
B_e	Y_{01}	$= 60.8380\ cm^{-1}$	H_e	Y_{03}	$= 4.25 \times 10^{-5}$
α_e	$-Y_{11}$	$= 3.0258$ "	η_e	Y_{13}	$= - .2 \times 10^{-5}$
γ_e	Y_{21}	$= .0345$ "			
δ_e	Y_{31}	$= - .0048 \pm .002$			

Most of these parameters agree very well with those obtained by Foltz et al (1966) and Fink et al (1965). The notable exceptions are the parameters π_e, H_e and η_e. The latter two parameters are more consistent with the values of H_v obtained by Herzberg and Howe (1959). The complete list of values for H_v is:

$H_0 = 4.1 \times 10^{-5} \pm 4 \times 10^{-5}\ cm^{-1}$
$H_1 = 3.9 \times 10^{-5} \pm 4 \times 10^{-6}\ cm^{-1}$
} present results

$H_2 = ---$
$H_3 = 3.72 \times 10^{-5}\ cm^{-1}$
$H_4 = 3.48 \times 10^{-5}$
$H_5 = 3.4 \times 10^{-5}$
$H_6 = 3.3 \times 10^{-5}$
} Herzberg and Howe

3.3 Absorption coefficients and polarizability matrix elements

The amount of absorption experienced by light passing through a sample of hydrogen gas can be expressed by

a simple loss equation:

$$I_{tr.}(\sigma) = I_{in.}(\sigma)\, e^{-B(\sigma)\ell}$$

where $B(\sigma)$ is the absorption coefficient and ℓ is the absorption path. The amount of absorption per unit length associated with a particular molecular transition equals:

$$B' = \frac{1}{\ell}\int_{\text{profile}} B(\sigma)d\sigma = \frac{1}{\ell}\int_{\text{profile}} \ln\left(I_{in}(\sigma)/I_{tr}(\sigma)\right) d\sigma$$

It is obtained theoretically by using "Fermi's golden rule":

$$B' = \frac{8\pi^3\sigma N}{hc}\,\left|\langle n \mid \vec{\mu} \mid n'\rangle\right|^2$$

where $\vec{\mu}$ is the dipole moment of the system, $|n'\rangle$ is the initial state, $|n\rangle$ is the final state, σ is the transition frequency, and N is the number of molecules per unit volume in the state $|n'\rangle$. The squares of the matrix elements of the dipole moment arising in the fundamental rotational-vibrational band are the following:

Transition J' ← J	Squared Matrix Element $\frac{1}{2J+1}\left(\sum_m \left|\mu_{\circ J'J}^{m'm}\right|^2\right)$
0 ← 0	$E^2(\alpha)^2_{01}$
1 ← 1	$E^2\left[(\alpha)^2_{01} + 8/225\,(\gamma)^2_{01}\right]$
2 ← 2	$E^2\left[(\alpha)^2_{01} + 8/315\,(\gamma)^2_{01}\right]$
3 ← 3	$E^2\left[(\alpha)^2_{01} + 16/675\,(\gamma)^2_{01}\right]$
2 ← 0	$E^2\ 4/45\,(\gamma)^2_{01}$
3 ← 1	$E^2\ 4/75\,(\gamma)^2_{01}$

(See Appendix A for the derivation of these matrix elements).

The number of particles per unit volume in each of the initial states is given by the Boltzmann distribution:

$$N = \rho N_0 \frac{(2J + 1)\, g\,(J)\, e^{-W_{vJ}/kT}}{\sum_{vJ} (2J + 1)\, g\,(J) e^{-W_{vJ}/kT}}$$

where ρ is the density of the gas in amagats, N_0 is Loschmitt's number and g(J) represents the nuclear statistic which is 3 for odd values of J (ortho hydrogen) and 1 for even values of J (para hydrogen). Values for N were computed at a temperature T = 295°K and including terms up to 2000 cm^{-1} in the partition function.

We find the following values:

$$N_{J=0} = \rho N_0 \times 0.1315$$
$$N_{J=1} = \rho N_0 \times 0.6617$$
$$N_{J=2} = \rho N_0 \times 0.1155$$
$$N_{J=3} = \rho N_0 \times 0.0866.$$

At a particular frequency σ, the value $B'/\rho E^2$ should be independent of ρ and E. However, Foltz et al (1966) have pointed out that the hydrogen lines exhibit considerable "saturation", and hence at large values of ρE^2 they observe smaller values of $B'/\rho E^2$ than at lower values of ρE^2. This trend in the values of $B'/\rho E^2$ can be noted in our observations shown in Table III where the product ρE^2 decreases monotonically from top to bottom. Even though the saturation effect is much less in our results (because most

measurements were taken at much lower values of ρE^2 than reported by Foltz et al) nevertheless $B'/\rho E^2$ was plotted as a function of ρE^2 and a value for $B'/\rho E^2$ at $\rho E^2 = 0$ was obtained for each spectral line by linear extrapolation. The slope of this linear dependence is significantly non-zero only for the stronger $Q_1(1)$ line. The extrapolated values are:

Line	$B'/\rho E^2$
$Q_1(0)$	$3.0 \pm .6 \times 10^{-15}$ cm^{-1}/(volt cm^{-1})^2 cm
$Q_1(1)$	$13.8 \pm 1.5 \times 10^{-15}$
$Q_1(2)$	$2.5 \pm .6 \times 10^{-15}$
$Q_1(3)$	$1.9 \pm .5 \times 10^{-15}$

From these values it follows by straightforward calculation that

$$\sqrt{(\alpha)^2_{01}} = 1.23 \pm .12 \times 10^{-25} \text{ cm}^3$$

$$\sqrt{(\alpha)^2_{01} + 8/225\ (\gamma)^2_{01}} = 1.16 \pm .08 \times 10^{-25} \text{ cm}^3$$

$$\sqrt{(\alpha)^2_{01} + 8/315\ (\gamma)^2_{01}} = 1.18 \pm .12 \times 10^{-25} \text{ cm}^3$$

$$\sqrt{(\alpha)^2_{01} + 16/675(\gamma)^2_{01}} = 1.21 \pm .12 \times 10^{-25} \text{ cm}^3$$

If we assume that $\gamma_{01} = .78$, as quoted by Church (1959), then it can be seen that it contributes only about 2 to 3% to $(\alpha)^2_{01}$ in each of the above expressions. Hence we can take the average value on the right hand side as a good estimate of α_{01}. We obtain:

$$\alpha_{01} = 1.20 \pm .1 \times 10^{-25} \text{ cm}^3.$$

A comparison of this value for α_{01} with values obtained both theoretically and experimentally follows:

Investigator	$\alpha_{01} \times 10^{25}$ cm^3
present	1.20 ± .1
Foltz et al (1966)	1.10
Church (1959)	.97
Crawford and MacDonald (1958)	.97
Ishiguro et al (1952)	1.39 (calculated).

It was not possible to obtain an estimate for the anisotropic matrix elements between the v = 0 and v = 1 vibrational states because the field induced S lines were obscured by the quadrupole S lines appearing in both the spectrum and the background.

It appears that the observed value of the isotropic polarizability is related to the resolution limit with which the spectra, from which it is evaluated, are recorded. We have observed that the line width of the Lorentz profile at about 30 amagat density is .06 cm^{-1}. Using this width, we can relate the product $\rho \ell E^2$ to the peak absorption from our data which yields:

$$\ln (I_0/I)_{max} = 1.54 \times 10^{-10} \rho \ell E^2$$

where ρ is the density in amagats, ℓ the absorption path and E the applied field in volts cm^{-1}. From this it can be seen that for example for the lowest value of $\rho \ell E^2$ used by Foltz near this density there is a peak absorption of about 83%.

Because of the non-linear relation between the absorption feature and ln (I_0/I) at such strong absorption, the broadening by the instrumental profile will have a strong influence on the value of the integral of the log ratio profile. This saturation effect should therefore disappear when the lines are fully resolved.

It has been found possible to obtain a rough estimate of the matrix element of the quadrupole moment between the v = 0 and v = 1 vibrational states from measurements of the quadrupole $S_1(1)$ line and from the quadrupole $Q_1(1)$ and $Q_1(2)$ lines which appear weakly in some "background" spectra obtained with the White cell. According to James and Coolidge (1938) the integrated absorption is related to the matrix element of the quadrupole moment $\mathcal{Q}$ by:

$$B' = \frac{1}{\ell} \int B(\sigma)d\sigma = \frac{4\pi^5\sigma^3 N}{5hc} |\langle n'|\mathcal{Q}|n\rangle|^2$$

From a spectrum taken at 2.56 amagat and for 50 m absorption path, we find:

$$B'_{Q_1(1)}/\rho = .0412 \times 10^{-3} \text{ cm}^{-1}/\text{amagat cm}$$

$$B'_{Q_1(2)}/\rho = .0036 \times 10^{-3} \text{ cm}^{-1}/\text{amagat cm (very poor signal to noise ratio)}$$

$$B'_{S_1(1)}/\rho = .0831 \times 10^{-3} \text{ cm}^{-1}/\text{amagat cm.}$$

The values for the $Q_1(1)$ and $S_1(1)$ lines agree very well with those obtained by Fink et al (1965). The value for the $Q_1(2)$ line is about 60% as much as the value obtained by Fink and will be ignored from here on. By straightforward arithmetic

we obtain for $\bar{Q}_{1-0}/e$ an average value of -90.8×10^{-3} Å^2. This compares with a value of -100×10^{-3} Å^2 obtained by Fink and -59.3×10^{-3} Å^2 as calculated from the work of James and Coolidge. More recent calculations seem to favour a value of about -120×10^{-3} Å^2 (Fink et al, 1965).

3.4 Frequency shift v.s. density

The variation of the central frequency of each line with changes in density is clearly shown in Figs. 16, 17, 18, 19 and 20. However, the density range over which these measurements were taken is relatively small and hence the data are not indicative of the behaviour of frequency shifts over the complete density range encountered in the gas phase. These frequency shifts have been studied more extensively by May et al (1961) and May et al (1964) in the Raman effect. They covered the density range from less than 100 amagat up to 800 amagat at different temperatures and with foreign gas mixtures.

For pure hydrogen at 300°K and 85°K May has postulated that the frequency shifts associated with isotropic Raman scattering are caused by perturbations of the vibrational motion only. For a quantitative interpretation of the shifts he expresses the frequency as a polynomial of degree two in the density:

$$[\sigma_{Q(J)}]_\rho = Q(J) + a_J \rho + b_J \rho^2$$

where Q(J) is the zero density frequency and ρ is the density in amagats.

He first points out that the J dependence of a_J suggests that a_J can be expanded into a constant term and a term that is proportional to the number of molecules in the initial rotational state, i.e.:

$$a_J = a_i + a_c\,(n_J/n).$$

The contribution of a_c to the shift could then be interpreted as a "coupling effect". The constants a_i, a_c and b_J are related to physically meaningful quantities by expressing the intermolecular potential as a power series expansion in the internuclear distances of an interacting pair of molecules. In this expansion it turns out that a_i is related to the linear term in the internuclear separation, b_J to the quadratic term, and a_c to the first cross term in the internuclear separations. By making use of the Lennard-Jones form of potential for the intermolecular potential, May has expressed a_i as the sum of an "attractive" and "repulsive" contribution, each consisting of a relatively large value giving a small but considerably temperature dependent difference a_i. With this model he then attempts to predict the coefficient b_J.

The frequency of each line as a function of the density was found by a least squares fit of all the observations to a quadratic function. The coefficients so obtained are listed in Table VII, along with the r.m.s. deviation.

TABLE VII

		present results		May et al		Foltz et al
J	$Q_1(J)$	$a_J \times 10^3$	$b_J \times 10^6$	$a_J \times 10^3$	$b_J \times 10^6$	$a_J \times 10^3$
0	4161.1653	$-2.44 \pm .14$	14 ± 5	-2.35	5.6	-2.34
1	4155.2543	$-3.58 \pm .11$	18 ± 4	-3.14	4.86	-3.25
2	4143.4664	$-2.62 \pm .22$	30 ± 8	-2.07	5.77	-2.02
3	4125.8696	$-1.42 \pm .45$	15 ± 15	-2.25	6.79	- .185

From a plot of a_J v.s. n_J/n the components a_i and a_c were obtained. On this plot it appears that a_J for $J = 3$ is considerably different from the predicted value for a_3 based on the relation given by May and using the present values of a_0, a_1 and a_2, as well as all the values quoted by May and Foltz (see Fig. 22). Then disregarding our value of a_3, we obtain:

$$a_i = -2.15 \pm 0.15 \times 10^{-3} \text{ cm}^{-1}/\text{amagat},$$

and

$$a_c = -2.35 \pm 0.25 \times 10^{-3} \text{ cm}^{-1}/\text{amagat}.$$

These values agree closely with those given by May and in fact the value for a_c is here somewhat closer to the value he predicts using the Lennard-Jones potential. The values obtained for the b coefficient are generally 3 to 4 times higher than those obtained by May over a wider density range. The reason for this discrepancy is not clear.

3.5 Line profiles

The full width at half the peak intensity (HIW) of

FIGURE 22

Graph showing linear frequency shift coefficient vs. relative population of initial states

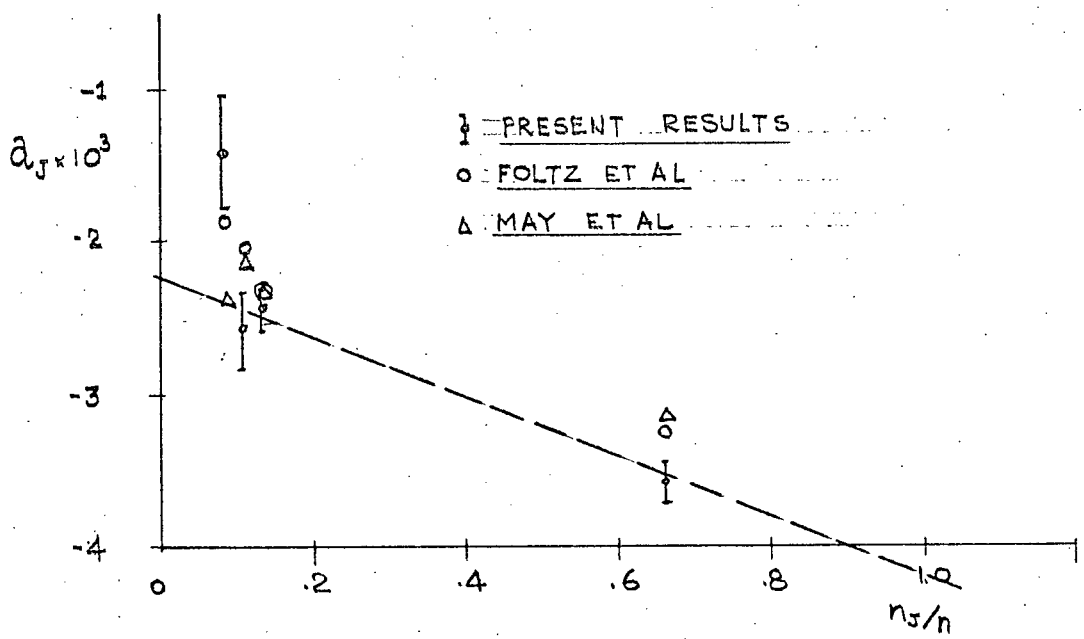
-1
-2
-3
-4
$a_J \times 10^3$
0
.2
.4
.6
.8
1.0
n_J/n
PRESENT RESULTS
FOLTZ ET AL
MAY ET AL

the profiles of the $Q_1(0)$, $Q_1(1)$, $Q_1(2)$ and $Q_1(3)$ lines have been deduced from the observed spectra over the density range from about 1.5 amagat to 28 amagat. These results are recorded in Table III and have been plotted in Figs. 16, 17, 18 and 19. Due to the poorer signal to noise ratio of the weaker lines there occurs a considerable scatter in the graph of line width v.s. density for these lines. However, in each case the trend of a reduction in line width towards lower density is unmistakable. It is also noteworthy that the minimum of line width (even for the uncorrected observed line width) is considerably less than the classical "doppler" width of these lines which equals 0.041 cm^{-1} at these frequencies. In the case of the $Q_1(1)$ line, which is about five times more intense than the other lines, it is possible to decompose the density dependence into a constant width plus a linearly increasing width plus some monotonically decreasing part which goes to zero between 3 and 4 amagat.

These observations agree qualitatively with measurements made by Cooper *et al* (1968) on the $S_0(0)$ and $S_0(1)$ lines in the Raman effect and by Lallemand *et al* (1966) on the stimulated Raman emission of the $Q_1(1)$ line. The narrowing to a width less than the doppler width of the $Q_1(1)$ line is, furthermore, consistent with an observation made by Rank and Wiggins (1963) on the quadrupole $Q_1(1)$ line. The narrowing of spectral lines due to pressure was first suggested by Dicke (1953). He pointed out that when many

elastic collisions occur during the displacement of a molecule over a distance λ, the wavelength of the radiation, the spectral distribution is determined by the self diffusion rate and not by the thermal velocities. Since the diffusion rate is much less than the mean thermal velocity, the resulting doppler shift will be less and hence a narrower line results. In practice, elastic collisions are usually accompanied by phase shifts in the oscillator amplitude, so that the coherence of the oscillations is reduced at each collision. This has the effect of reducing the length of the auto correlation function of the electric field of the radiation absorbed or emitted by these molecules, which consequently results in a broadening of the spectrum. Several authors (i.e. Galatry, 1961, Gersten and Foley, 1968 and Rautian and Sobel'man, 1966) have treated the case in which both doppler broadening and "collision" broadening take place. In each of these treatments the assumption was made that the perturbation caused by collisions is a definite function of time (assumption of classical path) so that the problem reduces, as was shown by Anderson (1954), to the problem of finding the autocorrelation function of the amplitude of the radiation field emitted or absorbed by the radiating system while it undergoes collisions. The spectrum is then taken to be the F.T. of the autocorrelation function. In taking into account the broadening due to collisional perturbations of the internal state of the molecule, the model of impact

broadening is used. This implies that the time during which the molecule is in "collision" with another molecule is small. It can be seen that both these assumptions are reasonable in the case of a hydrogen gas in thermal equilibrium at 300°K. The mean free path is about 1000 Å/atm. pressure and a wave packet representing the free translational motion at the average thermal speed extends over a few Angstrom units when the uncertainty in momentum is about 10% of its mean value. The effective range of the intermolecular potential for the hydrogen molecule is about 6 Å, hence at atmospheric pressure, and somewhat higher pressure, the "time of collision" is much less than the mean time between collisions. It appears therefore valid to compare in some detail the results obtained here with some of the predictions made by the above authors. The treatment of Rautian and Sobel'man (1966) seems most appropriate in that they treat a number of limiting cases that can be recognized as applicable here.

The spectrum is obtained by means of a Fourier transformation of the autocorrelation function of the amplitude of the light wave radiated by a moving oscillator. Following the treatment of Rautian and Sobel'man:

$$I(\omega) = \frac{1}{\pi} \operatorname{Re} \int \phi(\tau)\, e^{i\omega\tau}\, d\tau$$

where $\phi(\tau) = \langle E(t)^{*} E(t+\tau) \rangle$, ($\langle\ \rangle$ = time ave.)

and $E(t) = A(\omega_0)\, e^{i\omega_0 t + ik\, r(t)}$

r(t) is the location of the oscillator at a time t. It follows that

$$\phi(\tau) = A^2(\omega_0) \cdot e^{i\omega_0\tau} \langle e^{ikr(\tau)} \rangle$$

To simplify the discussion of the line profile, we set $A^2 = 1$ and $\omega_0 = 0$ after we have identified which spectral line is being studied. To find the expectation values above, Rautian and Sobel'man introduce a distribution function f (r, v, t; v_0), which gives the probability that a molecule moving a distance r in a time t acquires a velocity v when initially the particle was at the origin and its velocity was v_0. This distribution function satisfies the kinetic equation:

$$\frac{\partial f}{\partial t} + v \nabla f = S,$$

where S is the collision integral. If it is possible to solve for f, then it follows that

$$\phi(\tau) = \langle e^{-ikr(\tau)} \rangle = \int dv \int dv_0 \int e^{-ikr} f(r, v, \tau; v_0)\, dr$$

The autocorrelation function is also affected by changes in the phase of the amplitude of the oscillator as a result of collisions. This effect is taken into account by R. and S. in a manner similar to the above.

$$\phi_\psi(\tau) = \langle e^{i\Psi(\tau)} \rangle = \int e^{-i\Psi} f(\Psi, \tau)\, d\Psi$$

where $f(\Psi, \tau)$ is the distribution function for the phase after a time t. f is again obtained from the kinetic equation. The combined effect of motion and collisions can

then be treated in a unified way so that:

$$\Phi(\tau) = \langle e^{-ikr(\tau) - i\Psi(\tau)} \rangle = \int e^{-ikr - i\Psi} f(r,v,\Psi,\tau)\, dv\, dr\, d\psi$$

or

$$\Phi(\tau) = \int e^{-ikr}\, \tilde{f}(r,v,\tau)\, dv\, dr$$

where

$$\tilde{f} = \int e^{-i\Psi} f(r,v,\psi,\tau)\, d\Psi$$

We can now formulate the kinetic equation for the case of a combination of collision broadening and doppler broadening. We choose here the treatment of the "strong-collision" model which assumes that the velocity after collision is independent of the velocity before so that collisions will tend to establish an equilibrium distribution of velocities regardless of the initial velocity distribution. The characteristic time for this redistribution is of order $1/\nu$ where ν is related to the collision frequency. Also we choose the treatment of "statistical independence" in which it is assumed that the complex phase shift at a collision, $(\Gamma + i\Delta)$, is independent of the velocity of the emitting atom. This is applicable provided that ν as defined above is large (i.e. phase correlation remains after many collisions). Its validity can be verified by noting that statistical dependence leads to an assymmetric line profile which is not observed to within the limits of our experimental error. In this case, we have:

$$\frac{\partial \tilde{f}}{\partial t} + v \nabla \tilde{f} = -(\Gamma + i\Delta)\, \tilde{f} - \nu \left[\tilde{f} - w_m(v) \int \tilde{f}(r,v',t)\, dv' \right],$$

where $w_m(v)$ is the equilibrium distribution of velocities. The equation is solved by R. and S. by making use of the Fourier transform method which yields directly the space-time Fourier transform of the distribution function and which leads to the following expression for the line profile:

$$I(\omega) = \frac{1}{\pi} \operatorname{Re}\left[\frac{\int \frac{W(v)\,dv}{\nu+\Gamma-i(\omega-\Delta-kv)}}{1-\nu\int \frac{W(v)\,dv}{\nu+\Gamma-i(\omega-\Delta-kv)}}\right]$$

Since in this case the line is symmetric about the frequency Δ, we may for simplicity discuss the shape of the profile with $\Delta = 0$ (see section 3.4 for discussion of line shift). In the case that Γ and Δ are independent of v, the autocorrelation function is simply a product of the autocorrelation function associated with the doppler broadening and collision broadening. Since the "quenching" or radiation damping of the oscillator corresponds to a simple exponential decay of the autocorrelation function, independently of the motion or the collision processes, it can be simply taken into account by convolution in the spectrum. When the doppler broadening and the collision broadening are separated in the above expression,

$$I(\omega) = \int \frac{\Gamma/\pi \; d\omega'}{\Gamma^2 + (\omega-\omega')^2} \operatorname{Re}\left[\frac{1}{\pi}\,\frac{\int \frac{W(v)\,dv}{\nu-i(\omega'-kv)}}{1-\nu\int \frac{W(v)\,dv}{\nu-i(\omega'-kv)}}\right]$$

which is the convolution of a doppler profile and another

profile. Thus the collision broadening contribution consists simply of a Lorentz profile (we may add the effect of quenching to the width of this profile), and the doppler broadening consists of a more complex function in the general expression. We can treat the various limiting cases of this function and then find the effect of collision broadening upon it. Using the Maxwell distribution of velocities for $w_m(v)$, and in the first case taking $\gamma = 0$ (i.e. the initial velocities persist), $I(\omega)$ simply reduces to the convolution of the doppler profile with the Lorentz profile due to collision broadening. This is also the case when $\Gamma >> \gamma$ for $\gamma \neq 0$. The width at half intensity for the doppler profile is $\Delta\omega = 2\,\Delta\omega_D \sqrt{\ln 2}$. The detailed form of the doppler broadening contribution depends on the magnitude of γ relative to $\Delta\omega_D$. The parameter γ is proportional to the rate at which collisions take place in the gas. The proportionality constant depends on the nature of the collisions. For strong collisions during which the velocity changes considerably, it may be taken equal to the number of collisions per second. However, in weak collisions there may be several collisions before the velocity changes substantially. In whatever manner γ is defined, it is reasonable to assume that γ increases linearly with the density of the gas so that at different densities the different forms of the doppler profile should become apparent.

When $\gamma >> \Delta\omega_D$ ($\Delta\omega_D = 0.025$ cm^{-1} for hydrogen), the

central part of the doppler profile (for $\omega^2 << \nu^2$) takes on the simple dispersion form,

$$I_d(\omega) = \frac{1}{\pi} \frac{\gamma_d}{\omega^2 + \gamma_d^2}$$

where $\gamma_d = \frac{\Delta\omega_D^2}{2\nu}$.

From this we can deduce a value for ν by noting that when the monotone decreasing component of the line width in Fig. 17 is much less than 0.025 cm^{-1} all components of the profile are Lorentz profiles. This being the case the total width of the observed spectrum is simply the sum of the widths of the individual components. It is found from the observed data that in the range from 2 to 3 amagat, $2\gamma_d \leq .006$ cm^{-1} amagat. It follows that,

$$\nu = \frac{.025^2}{.006} \text{ cm}^{-1} \text{ amagat}^{-1}.$$

Expressing τ_v (the characteristic time of velocity change) in terms of $1/\nu c$, one finds:

$$\tau_v = 3.3 \times 10^{-10} \text{ sec amagat}$$

This may be compared with the mean time between collisions which is,

$$\tau_c = .6 \times 10^{-10} \text{ sec amagat.}$$

Thus the correlation of velocity extends over about six collisions. With this value for ν as a function of density it can be seen that the assumption $\nu >> \Delta\omega_D$ is valid over the

entire range of densities studied in this work. Rautian and Sobel'man further observe that when $\gamma >> \Delta\omega_D$, the profile is expected to vary as $1/\omega 4$ in the wings, as opposed to $1/\omega^2$ for the dispersion profile. However, this ω^{-4} dependence occurs only for $\omega > \gamma$. In the observed spectra the ω^{-4} dependence should start at about 0.1 cm^{-1} away from the center of the profile at 1 amagat density and this value increases linearly with density. This is too far removed from the center of the line to be studied, because the signal to noise ratio is not adequate. It is expected then that over the density range covered here, the line profile should be a dispersion profile. This is confirmed from a detailed comparison such as is shown in Fig. 21 applied to all spectral lines obtained. These observations agree qualitatively with predictions made by Gersten and Foley (1968) whereas the treatment of Galatry (1961) is less applicable here.

The following is a list of collision broadening coefficients obtained from the slope of the line width as a function of density:

$Q_1(0)$ .003 cm^{-1}/amagat

$Q_1(1)$ .0021 cm^{-1}/amagat

$Q_1(2)$ .0036 $\pm$ 3 x 10^{-4}

$Q_1(3)$ .0055 $\pm$ 5 x 10^{-4}.

4. Conclusions

The infrared absorption spectrum of hydrogen gas in a static electric field has been investigated at high resolution using an interferometric method. More precise frequencies have been obtained than those reported in the literature, which has permitted the evaluation of improved molecular constants. The phenomenon of collisional line broadening was observed and was studied in some detail. It was possible to compare the measurements with recent theoretical predictions. From the intensities of the induced lines it was possible to deduce values for the matrix element of the polarizability of hydrogen. The value obtained is higher than previously reported values, and this is attributed to our more accurate measurement of the line profiles.

The spectra obtained using the interferometer have been of good quality, being given the high resolution at which the measurements have been made. Nevertheless, the signal to noise ratio in the spectra has been poorer than one might have expected, and the reason for this has not been unambiguously established. It probably has to do with dynamical characteristics of the detector under strong illumination of the inevitably large flux in the continuous background spectrum; there has not been time to investigate this point thoroughly.

In order to improve the precision of the frequency determinations in future experiments using this apparatus,

several modifications should be carried out. The most obvious one is the installation of the entire optical path in a vacuum chamber. The second is the adoption of a servo control on the laser used as a frequency reference. It is clear, furthermore, that the laser actually used should be calibrated against a standard, because there are small differences in the frequency from laser to laser. Lastly, a more precise scanning mechanism should be constructed for the interferometer to reduce the speed fluctuations of the moving mirrors.

This work can obviously be extended to other homonuclear diatomic molecules such as D_2, N_2 and O_2. It would also be of interest to measure the weak allowed rotation-vibration spectrum of HD. In addition, some further work remains to be done with H_2 itself, particularly measurements at densities below 1 amagat. Also it would be of interest to measure the spectrum of pure parahydrogen, because one might expect that the collisional broadening would be slightly less pronounced.

If these investigations are carried out, some further work should be done on the multiple pass White cell, which in the form described in the thesis did not really live up to our expectations. In particular the gap between the electrodes is too large for the power supplies available, and it was difficult to attain adequately large field strengths.

BIBLIOGRAPHY

Anderson, P.W., 1954. J. Phys. Soc. Japan, 9, 316.

Brannon, P.J., Church, C.H. and Peters, C.W., 1968. J. Mol. Spectry, 27, 44.

Buijs, H.L. and Gush, H.P. 1967. "Colloque international du Centre National de la Recherche Scientifique", # 161 (April '66).

Church, C.H. 1959. Technical report no. 1, The University of Michigan.

Clark, J.B., Aitken, A.C. and Connor, R.D., "Physical and Mathematical tables", revised edition, 1957.

Condon, E.U. 1932. Phys. Rev. 41, 759.

Cooley, J.W. and Tukey, J.W., 1965. Math Comp. 19, 297.

Cooper, V.G., May, A.D., Hara, E.H. and Knapp, H.F.P., 1968. Can. J. Phys., 46, 2019.

Crawford, M.F. and Dagg, I.R., 1953. Phys. Rev., 91, 1569.

Crawford, M.F. and MacDonald, R.E., 1958. Can. J. Phys. 36, 1022.

Dicke, R.H., 1953. Phys. Rev., 89, 472.

Dunham, J.L. 1932. Phys. Rev., 41, 721.

Edlen, B., 1966. Metrologia 2, #2, 71.

Engelhard, E., 1966. Z. Angew. Phys., 20, 404.

Fink, U., Wiggins, T.A. and Rank, D.H. 1965. J. Mol. Spectry, 18, 384.

Foltz, J.V., Rank, D.H. and Wiggins, T.A., 1966. J. Mol. Spectry, 21, 203.

Galatry, L., 1961. Phys. Rev., 122, 1218.

Gersten, J.I. and Foley, H.M., 1968. J.O.S.A., 58, 933.

Herzberg, G., 1950. "Spectra of Diatomic Moleculed", Van Nostrand Co.

Herzberg, G. and Howe, L.L. 1959. Can. J. Phys., 37, 636.

Ishiguro, E., Arai, T., Mizushima, M. and Kotani, M. 1952. Proc. Phys. Soc. London A65, 178.

James, H.M. and Coolidge, A.S., 1938. Astrophys. J., 87.

Lallemand, P., Simova, P. and Bret, G. 1966. Phys. Rev. Letters, 17, 1239.

May, A.D., Degen, V., Stryland, J.C. and Welsh, H.L. 1961. Can. J. Phys., 39, 1769.

May, A.D., Varghese, G., Stryland, J.C. and Welsh, H.L. 1962. Can. J. Phys., 42, 1058.

Mielenz, K.D., Neffen, K.F., Gillilland, K.E., Stephens, R.B. and Zipin, R.B. 1965. Appl. Phys. Letters, 7 # 10

Mielenz, K.D., Neffen, K.F., Rowley, W.R.C., Wilson, D.C. and Engelhard, E., 1968. Applied Optics, 7, 289.

Rank, D.H. and Wiggins, T.A., 1963. J. Chem. Phys., 39, 1348.

Rautian, S.G. and Sobel'man, I.I., 1966. Uspecki Fiz. Nauk. 90, 209.

Stoicheff, B.P. 1957. Can. J. Phys., 35, 730.

Terhune, R.W., 1959. J. Mol. Spectry, 3, 138.

Vanasse, G.A. and Sakai, H. 1967. Progress in Optics, 6, chapter 7.

APPENDIX

Determination of the matrix elements of the components of the induced dipole moment between different rotational states.

We define a coordinate system (x'y'z') fixed with respect to the molecule and with the z' axis parallel to the internuclear axis. In the (x'y'z') system the components of the dipole moments are related to the field components via a diagonal polarizability matrix consisting of the principal polarizabilities of the hydrogen molecule,

$$\begin{pmatrix} \mu_{x'} \\ \mu_{y'} \\ \mu_{z'} \end{pmatrix} = \begin{pmatrix} \alpha_\perp & & 0 \\ & \alpha_\perp & \\ 0 & & \alpha_\parallel \end{pmatrix} \begin{pmatrix} E_{x'} \\ E_{y'} \\ E_{z'} \end{pmatrix}$$

The components of the dipole moment in a laboratory fixed frame (xyz) may be obtained using the rotation matrix $R(\alpha,\beta,\gamma)$, α,β,γ being the Euler angles of a rotation which carries (xyz) into (x'y'z'). We find,

$$\begin{pmatrix} \mu_x \\ \mu_y \\ \mu_z \end{pmatrix} = R \begin{pmatrix} \alpha_\perp & & 0 \\ & \alpha_\perp & \\ 0 & & \alpha_\parallel \end{pmatrix} R^{-1} \begin{pmatrix} E_x \\ E_y \\ E_z \end{pmatrix}$$

where

$$R(\alpha,\beta,\gamma) = \begin{pmatrix} \cos\alpha & \sin\alpha & 0 \\ -\sin\alpha & \cos\alpha & 0 \\ 0 & 0 & 1 \end{pmatrix} \begin{pmatrix} \cos\beta & 0 & \sin\beta \\ 0 & 1 & 0 \\ -\sin\beta & 0 & \cos\beta \end{pmatrix} \begin{pmatrix} \cos\gamma & \sin\gamma & 0 \\ -\sin\gamma & \cos\gamma & 0 \\ 0 & 0 & 1 \end{pmatrix}$$

Since we require the matrix elements of the induced dipole moment between wave functions consisting of spherical harmonics, it is more convenient to express the components of the dipole moment in the set of spherical basis vectors:

$$\begin{pmatrix} \mu_{-1} \\ \mu_0 \\ \mu_1 \end{pmatrix} = U^{-1} \begin{pmatrix} \mu_x \\ \mu_y \\ \mu_z \end{pmatrix} \quad \text{where } U = \frac{1}{\sqrt{2}} \begin{pmatrix} 1 & 0 & 1 \\ i & 0 & -i \\ 0 & \sqrt{2} & 0 \end{pmatrix}$$

From this it follows that,

$$U^{-1} \begin{pmatrix} \mu_x \\ \mu_y \\ \mu_z \end{pmatrix} = U^{-1}R \begin{pmatrix} \alpha_\perp & & 0 \\ & \alpha_\perp & \\ 0 & & \alpha_\parallel \end{pmatrix} R^{-1}U \begin{pmatrix} E_{-1} \\ E_0 \\ E_1 \end{pmatrix}$$

It is also customary to express the diagonalized polarizability matrix in two parts: the isotropic polarizability and the anisotropic polarizability:

$$\begin{pmatrix} \alpha_\perp & & 0 \\ & \alpha_\perp & \\ 0 & & \alpha_\parallel \end{pmatrix} = \left(\frac{2\alpha_\perp + \alpha_\parallel}{3}\right) \begin{pmatrix} 1 & & 0 \\ & 1 & \\ 0 & & 1 \end{pmatrix} + \left(\frac{\alpha_{11} - \alpha_\perp}{3}\right) \begin{pmatrix} -1 & & 0 \\ & -1 & \\ 0 & & 2 \end{pmatrix}$$

where α is the isotropic polarizability and where γ is the anisotropy of the polarizability. We note that $U^{-1}R\,U = D^1(\alpha,\beta,\gamma)$ and $URU^{-1} = D^1(\alpha,\beta,\gamma)^\dagger$ hence,

$$\begin{pmatrix}\mu_{-1}\\ \mu_0\\ \mu_1\end{pmatrix} = \begin{pmatrix}E_{-1}\\ E_0\\ E_1\end{pmatrix} + \gamma/3\ D^1(\alpha,\beta,\gamma)\ U^{-1}\begin{pmatrix}-1 & & \\ & -1 & \\ & & 2\end{pmatrix} UD^1(\alpha,\beta,\gamma)^{\dagger}\begin{pmatrix}E_{-1}\\ E_0\\ E_1\end{pmatrix}$$

where

$$U^{-1}\begin{pmatrix}-1 & & \\ & -1 & \\ & & 2\end{pmatrix} U = \begin{pmatrix}-1 & & \\ & 2 & \\ & & -1\end{pmatrix}$$

Then evaluating $D^1(\alpha,\beta,\gamma)\begin{pmatrix}-1 & & \\ & 2 & \\ & & -1\end{pmatrix} D^1(\alpha,\beta,\gamma)^{\dagger}$ from an expression for D^1 given by Tinkham it is seen that γ appears only in expressions like $e^{-i\gamma} \times e^{i\gamma} = 1$, and the resulting functions of α and β can be written as spherical Harmonics of order 2. Hence,

$$\begin{pmatrix}\mu_{-1}\\ \mu_0\\ \mu_1\end{pmatrix} = \begin{pmatrix}E_{-1}\\ E_0\\ E_1\end{pmatrix} + \frac{\gamma}{3}\sqrt{\frac{4\pi}{5}}\begin{pmatrix}Y_{2,0} & -\sqrt{3}\,Y_{2,-1} & -\sqrt{6}\,Y_{2,-2}\\ \sqrt{3}\,Y_{2,1} & 2\,Y_{2,0} & \sqrt{3}\,Y_{2,-1}\\ \sqrt{6}\,Y_{2,2} & -\sqrt{3}\,Y_{2,1} & -Y_{2,0}\end{pmatrix}\begin{pmatrix}E_{-1}\\ E_0\\ E_1\end{pmatrix}$$

It is always possible to choose the xyz coordinate system such that $E = E_0$. Then the components of the dipole moments are:

$$\mu_{-1} = \frac{-\gamma}{3}\sqrt{\frac{4\pi}{5}}\ Y_{2,-1}\ \sqrt{3}\ E_0$$

$$\mu_0 = \alpha E_0 + \frac{\gamma}{3}\sqrt{\frac{4\pi}{5}}\ Y_{2,0}\ 2\ E_0$$

$$\mu_{+1} = \frac{\gamma}{3}\sqrt{\frac{4\pi}{5}}\ Y_{2,1}\ \sqrt{3}\ E_0$$

We must now evaluate the matrix elements for these components of the induced dipole moment in the direction of

the electric field of the incident radiation. In all the work presented here, the incident light was plane polarized parallel to the static field. Thus we require,

$$\langle Y_{J'}^{m'} \mid \mu_0 \mid Y_J^m \rangle = \alpha E_0 \langle Y_{J'}^{m'} \mid Y_J^m \rangle + \frac{2}{3} \gamma E_0 \sqrt{\frac{4\pi}{5}} \langle Y_{J'}^{m'} \mid Y_2^0 \mid Y_{J'}^m \rangle$$

The first term on the right hand side equals $\alpha E_0 \delta_{JJ'} \delta_{mm'}$. The second term can be evaluated by making use of the Wigner-Eckart theorem which allows us to express these matrix elements as a product of the appropriate Clebsch-Gordan coefficient and a "reduced matrix element" which is independent of m and m'. We find the following explicit expression for the reduced matrix element in terms of a C-G coefficient and a J dependent factor,

$$\mu_{0\ J'J}^{m'm} = \alpha E_0 \delta_{J'J} \delta_{m'm} + \frac{2}{3} \sqrt{\frac{4\pi}{5}} E_0 \left(\frac{5(2J'+1)}{4\pi(2J+1)}\right)^{\frac{1}{2}} C(J'2J;000) \times C(J'2J; m'0m).$$

From this it is apparent that we have the selection rules $m' = m$, $J' = J$ for the isotropic contribution and $|J-2| \leq J' \leq J+2$ for the anisotropic contribution. Also $C(J'2J;000)$ is zero when $J' = J \pm 1$ so that $J' = J$ or $J \pm 2$ and $J' = 0$ to $J = 0$ is not allowed for the anisotropic part.